Linking magmatic processes and magma chemistry during the post-glacial to recent explosive eruptions of Ubinas volcano (southern Peru)

Pablo Samaniego, Marco Rivera, Nélida Manrique, Federica Schiavi, François Nauret, Céline Liorzou, Marie-Anne Ancellin

HAL Id: hal-02997285

https://uca.hal.science/hal-02997285

Submitted on 10 Nov 2020

1 **Linking magmatic processes and magma chemistry during the post-glacial to recent**

2 **explosive eruptions of Ubinas volcano (southern Peru)**

3

4 Pablo Samaniego[1*], Marco Rivera[2], Nelida Manrique[3], Federica Schiavi[1], François Nauret[1],

5 Céline Liorzou[4], Marie-Anne Ancellin[1]

6

7 [1] Université Clermont Auvergne, CNRS, IRD, OPGC, Laboratoire Magmas et Volcans, F-63000 Clermont-

8 Ferrand, France

9 [2] Instituto Geofísico del Perú, Observatorio Vulcanológico del Sur, Manzana B, Lote 19, Urb. La Marina, Cayma,

10 Arequipa, Peru

11 [3] Observatorio Vulcanológico del INGEMMET, Dirección de Geología Ambiental y Riesgo Geológico, Urb.

12 Magisterial B-16, Umacollo, Arequipa, Peru

13 [4] Laboratoire Géosciences Océan, Institut Universitaire Européen de la Mer, Université de Bretagne Occidentale,

14 Rue Dumont d'Urville, 29280 Plouzané, France

15

16 * Corresponding author:

17 Pablo Samaniego, pablo.samaniego@ird.fr, ORCID 0000-0003-1169-3503

18 Laboratoire Magmas et Volcans, Université Clermont Auvergne - CNRS - IRD, OPGC, Campus Universitaire

19 des Cézeaux, 6 Avenue Blaise Pascal, TSA 60026 - CS 60026, 63178 Aubière, France

20

21

22

Abstract

Understanding the links between the magma differentiation processes, the magma plumbing system and the magma composition at arc volcanoes is of paramount importance for volcanic hazard assessment. In this work we focus on the post-glacial, Holocene, historical, and recent eruption products of Ubinas volcano (Peru), which display an overall decrease in silica content from the older, plinian (VEI 3-5), rhyolitic eruptions (69-71 wt.% SiO_2) to the historical and recent (2006-2009, 2013-2017), vulcanian (VEI 1-2) basaltic andesitic eruptions (55-57 wt.% SiO_2). Based on a comprehensive study of the major and trace elements and the Sr-Nd-Pb isotopes, we conclude that this temporal pattern reflects the evolution of the Ubinas magmas in the middle-to-upper crust by a coupled Assimilation-Fractional Crystallization (AFC) process involving a cumulate composed of plagioclase, amphibole, clinopyroxene, orthopyroxene and Fe-Ti oxides, with minor amounts of olivine and biotite at the mafic and felsic end-members, respectively. Upper crustal assimilation is limited to 5-8 vol.%, but the overall radiogenic Sr-Nd-Pb signature of the Ubinas magmas requires a larger crustal component, which must therefore occur at middle to lower crustal depths. The petrology of the Ubinas magmas also points to an overall increase in P-T conditions: the large Holocene dacitic and rhyolitic eruptions record temperatures ranging from 800 to 850ºC and pressures in the range of 200-400 MPa, whereas the historical and recent (2006-2009, 2013-2017) basaltic andesitic eruptions provide higher temperatures and pressures (1000ºC, >300-400 MPa). Overall, the thermo-barometry, phase equilibrium and geochemical constraints allow us to propose the existence of a middle-to-upper crust magma column composed of a highly crystalline magma mush containing batches of liquid magma, which seems to be continually recharged from deeper levels. On the basis of the petrological nature of the historical basaltic andesitic eruptions (*CE* 1667, 2006-2009, 2013-2017), we postulate that during the last centuries, Ubinas experienced a recharge-dominated process, with no evidence for a rejuvenation of the silica-rich reservoir that fed the large Holocene dacitic to rhyolitic eruptions. This study highlights the importance of detailed petrological studies of Holocene sequences at explosive arc volcanoes in order to constrain the magmatic processes and conditions that control large explosive eruptions.

Keywords: Ubinas, Peru, arc volcanoes, recharge, thermobarometry, magma plumbing system

1. Introduction

Understanding the occurrence of explosive eruptions involving intermediate and silica-rich magmas (i.e. andesites, dacites and rhyolites) in arc volcanoes is of paramount importance for volcanic hazard assessment. It is widely accepted by the scientific community that primitive arc magmas result from partial melting of a source located in the mantle wedge which was previously metasomatized by fluids or melts derived from the subducted slab (Kelemen et al., 2014; Turner et al., 2016; Schmidt and Jagoutz, 2017). These magmas display a large geochemical heterogeneity related to the nature of their magma sources together with the fluid/melt transport in the mantle wedge (Grove et al., 2003; Rawson et al., 2016). Primitive arc magmas (mostly magnesium-rich basalts or basaltic andesites) ascend through the mantle wedge and stagnate at different levels in the arc crust, where they are modified by various non-exclusive physical and chemical processes. As a result, intermediate and silica-rich magmas are generated by a complex sequence of petrogenetic processes that include fractional crystallization, crustal assimilation, and magma mixing (Hildreth and Moorbath, 1988; Annen et al., 2006; Lee and Bachmann, 2014). On one hand, there is a large amount of geochemical and experimental data showing that andesites (and more differentiated liquids) are by-products of basalt crystallisation (Sisson et al., 2005; Blatter et al., 2013; Nandedkar et al., 2014; Ulmer et al., 2018). In addition, following the seminal work of Hildreth and Moorbath (1988), the deep arc crust is considered as a dynamic zone in which the process of melting, assimilation, storage and homogenisation (the so-called MASH model) are actively at work. This model has been corroborated by numerical and physical arguments (*cf.* Annen et al., 2006; Jackson et al., 2018). On the other hand, the paucity of intermediate (andesitic) composition melt inclusions compared to the overwhelming abundance of these compositions as bulk-rock erupted products suggests that magma mixing between silica-poor (primitive) and silica-rich (differentiated) magmas is a common process during andesite genesis (Eichelberger et al., 2006; Reubi and Blundy, 2009; Kent et al., 2010; Schiano et al., 2010). These models are probably end-member situations at work at different places in the arc crust. Thus, the magmatic plumbing systems that feed active volcanoes are considered to be vertically-elongated zones consisting of a mixture of solid phases and interstitial melt, in which ephemeral magma accumulation occurs (Cashman et al., 2016; Bachmann and Huber, 2016; Jackson et al., 2018). This model of *trans-crustal magmatic systems* rests on theoretical, geophysical, experimental petrology and geochemical arguments, and challenges the classic view of melt-dominated magma chambers. It accounts for the different compositional ranges observed in arc volcanoes as well as the overwhelming evidence for a multi-stage, polybaric sequence of crystallization for most arc magma suites.

81   Arc volcanoes show variable compositional trends on a timescale of hundreds to thousands of years. Some

82   arc volcanoes display homogeneous basaltic andesitic to andesitic magmas [e.g. Sangay (Monzier et al., 1999) and

83   Reventador (Samaniego et al., 2008) volcanoes in Ecuador, Arenal in Costa Rica (Ryder et al., 2006), Merapi in

84   Indonesia (Gertisser and Keller, 2003)]; whereas others are broadly dacitic magma systems [e.g. Mount St. Helens

85   (Blatter et al., 2017), Pinatubo (Newhall and Punongbayan, 1995), Guagua Pichincha (Samaniego et al., 2010),

86   Huaynaputina (Thouret et al., 1999)]. There are also arc volcanoes that mostly erupt andesitic magmas with scarce

87   eruptions involving silica-rich magmas during sporadic (albeit larger) events [e.g. Colima in Mexico (Luhr and

88   Carmichael, 1990; Robin et al., 1991; Macias et al., 2017), Tungurahua in Ecuador (Samaniego et al., 2011;

89   Andujar et al., 2017; Nauret et al., 2018)]. Lastly, some arc volcanoes display temporal geochemical variations,

90   for instance Cotopaxi volcano in Ecuador (Hall and Mothes, 2008; Garrison et al., 2011; Martel et al., 2018),

91   where larger rhyolitic eruptions transitioned to smaller andesitic events. This is also the case for Ubinas volcano

92   in southern Peru, which is characterized by a temporal geochemical trend showing a progressive decrease in silica

93   content over the last few thousand years (Thouret et al., 2005; Rivera et al., 2014), from pre-Holocene, large (VEI

94    $\geq$ 4) plinian eruptions involving rhyolitic magmas to the historical and recent, small-to-moderate (VEI 1-2)

95   vulcanian events that involve basaltic andesitic magmas.

96   In this study, we performed a detailed mineralogical and geochemical study that includes whole-rock

97   major, trace element and Sr-Nd-Pb isotopic analyses, as well as a comprehensive petrogenetical and thermo-

98   barometric study of a succession of explosive deposits covering the post-glacial, historical and recent eruptive

99   chronology of Ubinas. These data allow us to identify the main magmatic processes responsible for the diversity

100   of Ubinas magmas, as well as to petrologically image the magmatic plumbing system during the large eruptions

101   involving silica-rich magmas and the smaller events involving silica-poor magmas. These findings will contribute

102   to the hazard assessment at this active volcano of the Andean Central Volcanic Zone (CVZ). More generally, this

103   case-study provides constraints to discuss the magma processes at work at other arc volcanoes that display large

104   compositional ranges over relatively short time intervals (several thousands of years).

105

2. Eruptive chronology

107   Ubinas volcano (16º 22'S, 70º 54'W, 5672 meters above sea level – m a.s.l.), located ~75 km east of

108   Arequipa (Fig. 1), is the most active volcanic centre of the Peruvian arc, and together with Sabancaya and Lascar

109   are amongst the most active volcanoes in the Andean Central Volcanic Zone (CVZ). This segment of the Andean

110   arc developed on a thick continental crust (up to 65-75 km thick, Ryan et al., 2016) and results from the subduction

of the Nazca plate below the South-American lithosphere. Ubinas has experienced at least 27 low-to-moderately explosive (VEI 1-3) eruptions in historical and recent times (i.e. from the beginning of the Spanish conquest in ~1532 *CE* to the present day) (Siebert et al., 2010; Rivera et al., 2014). The eruptive chronology of Ubinas was studied in detail by Thouret et al. (2005) and Rivera (2010), who defined two successive edifices (Ubinas I and Ubinas II). The older, mostly effusive Ubinas I volcano was constructed by the emplacement of andesitic and dacitic lava flows from around 450 to 370 ka, and suffered a large sector collapse at the end of its growth. The younger Ubinas II volcano was constructed on top of the older edifice over the last 370 ka and consists of andesitic and dacitic lava flows and domes and thick successions of block-and-ash-flow deposits that infill the Ubinas valley to the south. It forms a truncated cone with a summit caldera (1x1.5 km), which testifies to intense explosive activity in Late Pleistocene times. Based on the stratigraphy, Thouret et al. (2005) suggested that this summit caldera was formed between 25 and 10 ka by a sequence of large explosive eruptions responsible for a thick succession of plinian tephra fall deposits. Geochronological data from these deposits are infrequent due to the scarcity of organic material for radiocarbon dating as a consequence of the extremely arid weather conditions of the Central Andes. However, rough temporal constraints come from stratigraphic correlations with distal tephra layers found at Laguna Salinas, 25-30 km west of Ubinas (Juvigné et al., 1997). Based on these data, Thouret et al. (2005) considered that the basal tephra of the caldera-related succession is older than 14 ka. In any case, these eruptions occurred after the Late Glacial Maximum (LGM), dated at 17-25 ka in this part of the Andes (Smith et al., 2008; Bromley et al., 2009; Blard et al., 2014).

Figure 1

The post-glacial eruptive succession at Ubinas (Fig. 2a) comprises 10-15 m-thick plinian tephra fallout deposits that crop out in the southern and south-eastern part of the cone at a distance of up to 15 km from the summit. Around the hamlet of **Sacuhaya** (8-9 km south of the summit), at least seven pumice-and-lithics tephra layers were described. The basal layer is a 2-3 m-thick, rhyolitic white pumice deposit (Fig. 2b) that correlates with the distal Laguna Salinas ash fallout deposit (see above). In this cross-section, we found six additional, 10-100 cm-thick tephra fallout layers, which correspond to the Holocene plinian activity of Ubinas (Fig. 2c). A charcoal sample collected from an ash-rich paleosol layer in the lower-middle part of this cross-section, directly below a 1 m-thick plinian fallout deposit (UBI-10-12 sample, Fig. 2c, 3a), was dated at 7480 ± 40 BP by Thouret et al. (2005). This date represents the only absolute age for this tephra succession. All these tephra layers

141 correspond to Ubinas post glacial activity, excepting a 10-15 cm-thick, white, fine lapilli, tephra fallout deposit

142 that blankets the region located to the south of Ubinas (samples UBI-10-15 and UBI-10-08, Fig. 3). Based on

143 tephra dispersal studies performed by Wright et al. (2017) and the chemical composition of these samples (see

144 below), we consider the source of this deposit being a different volcano than Ubinas. At ***Quebrada Infiernillos***

145 (5-6 km southeast of the summit), the tephra fallout deposits correlate with the middle-upper part of the Sacuhaya

146 cross-section. In addition, in this outcrop, we found the deposits of the last two plinian eruptions of Ubinas (VEI

147 4-5, Thouret et al., 2005; Siebert el al., 2010), which were dated at 980 ± 60 BP (Fig. 2a, d). During the fieldwork

148 performed for this study, we found at the base of these tephra fallout deposits, a >50 cm, ash-rich layer with

149 disseminated pumice fragments, containing non-carbonized branches that yielded an age of 1890 ± 70 BP (UBI-

150 15-03, GrA 65545, Center for Isotope Research, University of Groningen, The Netherlands). Given the

151 stratigraphic position of this sample (in the underlying ash-rich layer), we consider that this age represents the

152 oldest age limit for this eruption. Based on the previous and these new data, we consider that the last plinian

153 eruption at Ubinas occurred at 1-2 ka.

154   Eruptive activity in historical and recent times has been characterized by low-to-moderate (VEI 1-2)

155 vulcanian eruptions accompanied by long-lasting ash and gas emissions. The large eruption of this period occurred

156 in *CE* 1667 (Thouret et al., 2005; Siebert el al., 2010) and was characterized by a moderately explosive (VEI 3)

157 event that produced low-volume, scoria-rich pyroclastic flow deposits that outcrop on the upper part of the cone,

158 close to the caldera border (Fig. 2e). During the last two decades, Ubinas has experienced several eruptive periods

159 in 2006-2009, 2013-2017 and recently in 2019 (Fig. 1b, Fig. 2f). These eruptions show very similar patterns,

160 starting with a strong phreatic phase followed by intermittent vulcanian events that progressively waned over a

161 period of a few years (Rivera et al., 2010; 2014).

162

163 Figure 2

164

165 **3. Sampling and analytical methods**

166   Based on the comprehensive work of Thouret et al. (2005) and Rivera (2010) we sampled the key cross-

167 sections of Sacuhaya and Quebrada Infiernillos as well as the historical and recent eruptive products of the *CE*

168 1667, 2006-2009 and 2013-2017 eruptions (Fig. 2). Major and trace element concentrations of 33 new whole-rock

169 samples from the post-glacial eruptive events, including 8 samples from the historical and recent eruptions (*CE*

170 1667, 2006-2009, and 2013-2017), were analysed at the Laboratoire Geosciences Océan, Université de Bretagne

Occidentale (Brest, France). Agate-grinded powders were dissolved in HNO_3 and HF and then measured by ICP-AES (Inductively Coupled Plasma-Atomic Emission Spectroscopy), following the procedure of Cotten et al. (1995). Relative standard deviations are 1% for SiO_2 and $\leq$ 2% for the other major elements, and $\leq$ 5% for trace elements. To these data we added the major and trace element compositions of 24 samples previously published by Thouret et al. (2005) and Rivera et al. (2014). Sr, Nd and Pb isotopic ratios were measured at Laboratoire Magmas et Volcans (LMV), Université Clermont Auvergne (Clermont-Ferrand, France) for 15 samples that span the post-glacial activity of Ubinas. Sr and Nd data were obtained following the techniques described by Pin et al. (1994) and Pin and Santos Zalduegui (1997), using a TIMS and a MC-ICP-MS respectively. We include 10 Sr–Nd isotopic ratios published by Thouret et al. (2005), Rivera (2010) and Rivera et al. (2014), which were also analysed at LMV, following the same analytical procedure. Sr isotopic measurements were corrected for mass-fractionation using an exponential law and $^{86}Sr/^{88}Sr = 0.1194$ and normalized to the value of the NIST SRM987 standard ($^{87}Sr/^{86}Sr = 0.710245$). Nd isotopic measurements were corrected for mass fractionation using an exponential law and $^{146}Nd/^{144}Nd = 0.7219$ and normalized to the value of JNdi-1 standard ($^{143}Nd/^{144}Nd = 0.512100 \pm 5$ (2σ), n = 5). External reproducibility was monitored by repeated analyses of JNdi-1 standard ($^{143}Nd/^{144}Nd = 0.512097 \pm 10$ (2σ), n = 13). This value is equal, within error margins, to the proposed value for JNdi-1 standard. Pb isotopic ratios were determined following the methods described by Nauret et al. (2018), using a MC-ICP-MS at LMV. Pb isotope ratios were normalized to values of NIST SRM 981 given by Galer et al. (1998). Total procedural blanks are lower than 0.15 ng (n = 6), which is negligible compared to the amount of Pb loaded on the columns (200 to 500 ng). We used international standards (AGV2, BHVO2 and BIR-1) in order to test the reproducibility of our method. Values obtained for AGV-2 are $^{206}Pb/^{204}Pb = 18.870$; $^{207}Pb/^{204}Pb = 15.618$; $^{208}Pb/^{204}Pb = 38.546$ (n = 5), for BHVO-2: $^{206}Pb/^{204}Pb = 18.608$; $^{207}Pb/^{204}Pb = 15.536$; $^{208}Pb/^{204}Pb = 38.212$ (n = 2) and for BIR-1: $^{206}Pb/^{204}Pb = 18.848$; $^{207}Pb/^{204}Pb = 15.655$; $^{208}Pb/^{204}Pb = 38.489$ (n= 1). These results are in agreement with the international reference values. All measured Pb isotope compositions were corrected for mass fractionation by adding a solution of the NIST SRM 997 Tl standard to the sample before measurement. The new whole-rock major and trace elements and isotopic ratios are presented in Table 1. Sample locations are given in the electronic Supplementary material 1.

Major element compositions for minerals and matrix glasses of 11 representative samples of Ubinas eruptive products were analysed at the LMV, using a CAMECA SX-100 microprobe. The operating conditions for minerals were 15 kV accelerating voltage, 10–12 nA beam current, and 10 s counting time; whereas the matrix glass measurements were performed using a 15 kV accelerating voltage, 4-8 nA beam current, 5-10 μm beam size,

201 10 s counting time, and using international glass standards. With these operating conditions and given that alkali

202 elements measurements were performed first, we should avoid significant Na migration under the electron beam

203 (*cf.* Devine et al., 1995). Selected major elements composition of Ubinas minerals are presented in Tables 2, 3, 4,

204 5; whereas the entire dataset was included in the Supplementary material 2. In order to measure trace element

205 concentrations of selected Ubinas minerals, Laser-Ablation-ICP-MS analyses were performed on phenocrysts of

206 selected Ubinas samples, using a 193 nm Resonetics M-50E excimer laser coupled to an Agilent 7500cs ICP-MS.

207 The laser energy was about 3 mJ, with a pulse frequency of 2-3 Hz. The spot diameter was set at 60-80 μm and

208 the analysis time was 100 s after a background measurement (~30 s). The technique uses calcium as an internal

209 standard and measurements were calibrated relative to the NIST-612 glass. The glass standard BCR was also

210 measured to check the reliability of the results. Data treatment was performed on Glitter software (www.glitter-

211 gemoc.com). The typical analytical error for most trace elements is < 10%.

212 We measured the pre-eruptive water content on selected melt inclusions using a Renishaw InVia confocal

213 microspectrometer equipped with a 532 nm diode laser (200 mW output power), a Peltier-cooled CCD detector, a

214 motorized XYZ stage and a Leica DM2500 M optical microscope, at the LMV. The laser power was set to ~3

215 mW. A 2400 grooves/mm grating, a 100× objective and 20 μm slit aperture (high confocality setting) were used

216 for the analyses. These analytical conditions result in lateral spatial resolution of ~1 μm and spectral resolution

217 better than 1 cm^{-1}. Daily calibration of the spectrometer was performed based on the 520.5 cm^{-1} peak of Si. The

218 spectra were recorded in the wavenumber ranges from ~100 to 1350 cm^{-1} (alumino-silicate network domain) and

219 from ~3000 to 3800 cm^{-1} (water domain), using Wire 4.2 software. Acquisition times were 60-240 s and 120-480

220 s for the alumino-silicate and water domains, respectively. Spectra treatment was performed using PeakFit 4.0

221 software. For determination of water content in glasses, we used the external calibration procedure and a set of

222 hydrous glass standards with rhyolitic, andesitic, and basaltic compositions (see Schiavi et al. (2018) for details

223 about the method) that were analysed at the same conditions as the samples several times a day. All the analysed

224 glass inclusions contain "nanolites" of magnetite, as revealed by the presence of its main peak centred at ~ 670

225 cm^{-1} (Supplementary material 3). The intensity of the magnetite peak relative to the main glass band near 500 cm^{-}

226 ^{1} varies significantly among the samples (intensity ratio from 0.4 to 1.8). Di Genova et al. (2017) and Schiavi et

227 al. (2018) observed that the presence of magnetite dispersed in the glass causes underestimation of the water

228 content of the inclusion. Therefore, the estimated water contents are minimum values. The water contents are

229 weakly underestimated in inclusions whose spectra show a weak magnetite signal (band intensity ratios 0.4-0.5),

230 but they are strongly underestimated in inclusions with an intense magnetite peak (Supplementary material 4).

4. Petrological data

4.1. Whole-rock geochemistry

The post-glacial, historical and recent eruptive products of Ubinas form a continuous high-K magmatic trend, ranging from basaltic andesites to rhyolites (55-71 wt.% SiO_2; 2-4 wt.% K_2O, recalculated as anhydrous, Fig. 3). The most striking characteristic of this dataset is the overall decrease in silica content through time. At the base of the tephra succession, we have the older rhyolitic compositions (69-71 wt.% SiO_2) of the pre-Holocene eruption deposits, followed by several Holocene dacitic (62-69 wt.% SiO_2) tephra fall deposits. Above this is the andesitic (60-62 wt.% SiO_2) tephra fallout deposits that corresponds to the 1-2 ka plinian eruptions. The Ubinas stratigraphic succession terminates with the historical and recent eruptive products of basaltic andesitic compositions (55-57 wt.% SiO_2), that include those of the *CE* 1667, 2006-2009 and 2013-2017 eruptions (Fig. 3). A more detailed observation of this dataset reveals that the chemical variation is not uniform, there are two periods of silica-rich compositions in the middle (samples UBI-10-14, 16; Fig. 3), and in the upper part of the Holocene volcanic succession (the 1-2 ka eruption). Concomitantly with silica variations, the K_2O and some incompatible trace elements (e.g. Rb, Th) show also a decrease through time; whereas MgO concentrations, as well the compatible elements (e.g. Sr, Ni, Cr) display an overall increase from the older rhyolites to the younger basaltic andesites, up to a maximum for *CE* 1667 eruption products (Supplementary materials 5 and 6). We should highlight the presence of two samples that lie off the main trend (UBI-10-15 from Sacuhaya section, and UBI-10-08 from Quebrada Infiernillos section), which are represented by black dots in Fig. 3 and the other geochemical plots. Compared to the other tephra layers and for the same silica content, these samples display lower incompatible elements concentrations (e.g. K_2O, Rb, Th, La, Fig. 3 and 4; Supplementary materials 5 and 6).

Overall, the Ubinas magmatic series displays well-defined negative correlations for silica and most major elements (Fig. 4, Supplementary materials 5), except for Al_2O_3, and Na_2O that are highly scattered. Sr and the transition metals (e.g. Sc, V, Co, Cr, Ni) also show negative correlations with silica increase. Conversely, some trace elements (and K_2O) show fairly good positive correlations with silica, especially the Large-Ion Lithophile Elements (LILE; e.g. Rb, Th), while the High Field Strength Elements (HFSE; e.g. Nb and Zr) show a broad scatter. The Rare Earth Elements (REE) display a notable behaviour: the light REE (LREE; e.g. La, Ce) show no clear variation with silica increase, spanning over a wide range of values for the same silica content, whereas the Middle and Heavy REE (MREE and HREE; e.g. Nd, Sm, Yb) display clear negative correlations. As a result, REE ratios show temporal trends, such as a progressive decrease in La/Sm and increase in Sm/Yb or Dy/Yb ratios from

9

261   rhyolites to basaltic andesites (Supplementary materials 6). Lastly, the major and trace element variations have a

262   noticeable break-in-slope at 56-58 wt.% SiO_2, with the basaltic andesitic group (BA) on one side and a more

263   widespread andesitic-dacitic-rhyolitic group (ADR) on the other side. We keep this dichotomy for the forthcoming

264   sections of this manuscript.

265

266   Figure 3

267   Figure 4

268   Table 1

269

270   Sr and Nd isotopic data broadly display homogeneous values at the scale of the CVZ (Fig. 5a). In detail,

271     $^{87}Sr/^{86}Sr$ range between 0.70657 and 0.70707 with $^{143}Nd/^{144}Nd$ between 0.51228 and 0.51235 (Fig. 5b, Table 1).

272   These isotopic ratios are plotted far from the mantle domain represented by the MORB field and they display a

273   negative correlation in $^{87}Sr/^{86}Sr$ *vs.* $^{143}Nd/^{144}Nd$ diagram. We should stress that sample UBI-10-15 plots off the

274   trend with low $^{143}Nd/^{144}Nd$ and relatively high $^{208}Pb/^{204}Pb$ values. This characteristic confirms the interpretation

275   that this deposit does not correspond to Ubinas. Note that although we include these samples on the geochemical

276   plots, we exclude them from the subsequent analysis. Looking in detail, BA samples display the less radiogenic

277   values in Sr and the most radiogenic in Nd, although they display a variability that accounts for at least 50% of the

278   whole Ubinas isotopic variation (Fig. 5b). Surprisingly, the most radiogenic Sr values (and conversely the less

279   radiogenic Nd values) are displayed by some dacites (rather than rhyolites, Fig. 5b). On the whole, Sr-Nd isotopic

280   ratios define fairly good correlations with most differentiation indices (e.g. SiO_2, K_2O, Rb, Th; Supplementary

281   materials 7). All samples fall within the isotopic field of the Andean Central Volcanic Zone (Davidson et al., 1991)

282   and roughly display less radiogenic Sr compositions (Fig. 5a) than those of El Misti volcano (Rivera et al., 2017),

283   but similar to those of the Andahua monogenetic cones (Delacour et al., 2007). Pb isotopic data also display very

284   homogeneous values at the scale of the CVZ (Mamani et al., 2010). However, looking at in detail, they display a

285   quite large range of variation ($^{206}Pb/^{204}Pb$: 18.147-18.244; $^{207}Pb/^{204}Pb$: 15.610-15.616; $^{208}Pb/^{204}Pb$: 38.548-38.649;

286   Fig. 5c), with no well-defined linear correlations in $^{206}Pb/^{204}Pb$ *vs.* $^{207-208}Pb/^{204}Pb$ diagrams (Fig. 5d). In contrast to

287   the Sr-Nd isotopic data, the Pb isotopic ratios of Ubinas differ from those of the Andahua monogenetic cones,

288   plotting at lower $^{206}Pb/^{204}Pb$ and higher $^{207}Pb/^{204}Pb$ values (Fig. 5c).

289

290   Figure 5

4.2. Petrography and mineral chemistry

Blocks and bombs from the BA group are porphyritic, black to grey, dense to poorly vesiculated rocks bearing 20-25 vol.% phenocrysts of plagioclase, ortho- and clinopyroxene and Fe-Ti oxides, with scarce amphibole and olivine. On the contrary, the ADR samples are mostly phenocryst-poor (< 5 vol.%), highly vesiculated pumices with variable mineral assemblages. Andesitic samples contain plagioclase, amphibole, ortho- and clinopyroxene, Fe-Ti oxides and scarce phenocrysts of biotite, whereas dacites and rhyolites are composed of plagioclase, amphibole, biotite, and Fe-Ti oxides. Thus, the mineral assemblage changed concomitantly with magma chemistry from BA to ADR samples (Fig. 6).

Figure 6

Plagioclase is the most abundant phase in Ubinas samples. In BA group, plagioclase (10-20 vol.%) occurs as euhedral and subhedral phenocrysts showing a wide compositional range (An$_{35-80}$, Fig. 7, Table 2), sometimes within a single phenocryst (e.g. An$_{36-65}$, Rivera et al., 2014; and new unpublished data from 2006 and 2015 eruptive products). In spite of this diversity, most (~70%) phenocryst cores and rims display compositions between An$_{45}$ and An$_{65}$ (Fig. 7). On the basis of textural and chemical characteristics, we identified two different plagioclase populations in BA samples: (1) euhedral, non-altered phenocrysts with normal, oscillatory and reverse zoning patterns; and, (2) sieve-cored and sieve-ringed phenocrysts with frequent dissolution zones and clear overgrowth rims displaying strong reverse zoning (e.g. An$_{40-64}$). In the ADR samples, plagioclase is also the most abundant phase (5-15 vol.%), displaying clear (unaltered), euhedral to subhedral forms with also large compositional variations (e.g. An$_{33-72}$; Fig. 7) and frequent normal zoning patterns (e.g. An$_{65-40}$), while some phenocrysts display no chemical variation. We also found rare reversely zoned phenocrysts (e.g. An$_{46-51}$) as well as some inherited cores (e.g. An$_{70}$). We note that the peak for the An composition shifts from An$_{50-65}$ for BA to An$_{35-50}$ for ADR (Fig. 7). Although the compositional range observed in ADR is as large as those of for BA plagioclases, the phenocryst's rims display more restricted compositions in the ADR group (An$_{35-55}$ for dacites, and An$_{40-60}$ for rhyolites). Lastly, the large compositional range of plagioclases from both groups suggest that some of them should be considered as antecrysts (*cf.* Streck, 2008), i.e. the An-poor cores and rims in BA group, and the An-rich cores in ADR group.

Figure 7

11

321   Table 2

322

323   ***Amphibole*** phenocrysts are ubiquitous in Ubinas samples. They are an accessory phase (~1 vol.%) in BA

324   group, displaying anhedral forms with frequent opaque (black) reaction rims (*cf.* De Angelis et al., 2013), whereas

325   other phenocrysts are completely altered. They display homogeneous magnesium-hastingsite compositions

326   (according to the classification of Leake et al., 1997). In contrast, amphibole phenocrysts in the ADR samples are

327   much more abundant (2-5 vol.%), and appear as euhedral phenocrysts without any disequilibrium features. They

328   display wide compositional variations, spanning the magnesium-hastingsite, tschermakite and magnesium-

329   hornblende groups. The large compositional variation of Ubinas amphibole phenocrysts is summarized in an Al_2O_3

330   *vs.* Mg# diagram (Fig. 8a, Table 3). In this figure, amphibole from the BA samples show homogeneous, high-Al

331   contents (12.5-13.1 wt.% Al_2O_3) and relatively high Mg# (65-73) [where Mg# = 100 * Mg/(Mg + Fe^T) in mol.%,

332   and Fe^T is total iron as Fe^{2+}]. Amphiboles in andesites display intermediary and homogeneous Al contents (9.9-

333   11.0 wt.% Al_2O_3) and homogeneous Mg# values (66-68), whereas amphibole phenocrysts in dacites and rhyolites

334   span a large compositional range (7.0-12.7 wt.% Al_2O_3; Mg# 61-71). Such a broad chemical composition of

335   amphiboles is usually ascribed to changes in chemical and thermodynamic parameters such as melt composition,

336   pressure, temperature and redox state (Johnson and Rutherford, 1989; Schmidt, 1992; Bachmann and Dungan,

337   2002; Prouteau and Scaillet, 2003; De Angelis et al., 2013; Krawczynski et al., 2012; Erdmann et al., 2014; Kiss

338   et al., 2014). In order to constrain the role of the main parameters controlling amphibole chemistry, a substitution

339   analysis is usually performed (*cf.* Poli and Schmidt, 1992; Bachmann and Dungan, 2002). Fig. 8b and c show the

340   variation of three key parameters [^{IV}Al, ^{VI}Al and $(Na+K)^A$] that suggest a leading role for edenite (*ed*) substitution,

341   a valuable proxy for temperature variations. However, the variation observed in ^{VI}Al component also points out

342   for a role of the tschermakitic (*tk*) substitution, which is considered as a proxy for pressure variations. In addition,

343   Kiss et al. (2014) propose that the variations in Mg# coupled with the variation in Al content of amphiboles (Fig.

344   8a) could be used as a proxy for variation in melt composition.

345

346   Figure 8

347   Table 3

348   Table 4

349

350   ***Clinopyroxene*** phenocryts in BA samples (~5 vol.%) show diopsidic to augitic compositions (En_{38-47}-

351   Fs_{10-21}-Wo_{38-46}, Table 4, according to the classification of Morimoto et al., 1988), display euhedral forms, mostly

352   with reverse zoning patterns, although some phenocrysts show homogeneous compositions. The MgO content of

353   clinopyroxene, expressed by the Mg#, ranges from 65 to 82. There are also some inherited cores, which are mantled

354   by thin (10-50 μm), Mg-rich (Mg# 76-80) overgrowth rims. Clinopyroxene is also present as an accessory phase

355   (<1 vol.%) in andesitic and dacitic samples as phenocrysts or microphenocrysts with very homogeneous

356   compositions (Mg# 76-77).

357   ***Orthopyroxene*** phenocrysts appear to some extent (~2 vol.%) in BA group as well as in andesitic and

358   dacitic samples. They appear as euhedral phenocrysts, frequently associated with clinopyroxene. They have

359   enstatitic compositions (En_{65-71}-Fs_{24-34}-Wo_{2-4}, Table 4, according to the classification of Morimoto et al., 1988).

360   Slight differences in Mg# have been observed between orthopyroxenes from BA and andesites (70-76) and dacites

361   (67-70). We stress that orthopyroxene is absent in rhyolites.

362   ***Biotite*** phenocrysts are ubiquitous in rhyolites (2-4 vol.%), are much scarcer (1-2 vol.%) in dacites, and

363   are absent from more mafic rocks. Biotite appears as euhedral (up to 1-2 mm long) phenocrysts without reaction

364   rims or any other disequilibrium textures. They display homogeneous compositions with $Fe^{2+}/(Fe^{2+}+Mg)$ ratios of

365   0.33-0.36 and very restricted Mg# values (64-67, Table 3). These characteristics confirm these micas are classified

366   as biotites (according to the classification of Deer et al., 2013).

367   ***Fe-Ti oxides*** appear throughout the Ubinas magmatic series as microphenocrysts and microlites in the

368   matrix (1-2 vol.%) as well as inclusions in other mineral phases. They mostly correspond to titanomagnetite (6-18

369   wt.% TiO_2, Table 5), although rare ilmenite (37-38 wt.% TiO_2) crystals are also observed in some dacites. Rivera

370   (2010) also reports some rare ilmenite crystals in dacites and rhyolites of Ubinas.

371   ***Olivine*** appears only as an accessory phase (< 1 vol.%) in BA such as those of the 2006-2009 and 2013-

372   2017 eruptions. They are mostly subhedral or euhedral phenocrysts (up to 300-400 µm) or microlites with

373   homogeneous compositions (Fo_{66-78}, Table 5), and usually normal zoning patterns. Olivine phenocrysts frequently

374   show reaction rims composed of plagioclase, pyroxene, and Fe–Ti oxides, or more scarce orthopyroxene

375   overgrowth rims.

376   Lastly, some ***apatite*** microphenocrysts and microlites are found as inclusions in plagioclase and

377   amphibole, whereas ***zircon*** microlites occurs as inclusions in biotites.

378

379   Table 5

380

4.3. Trace elements in minerals

Trace element concentrations were measured in plagioclase, ortho- and clinopyroxene, and amphibole phenocrysts from three Ubinas samples, a basaltic andesite (UBI-10-18B), an andesite (UBI-10-01) and a rhyolite (UBI-10-10C). Results are plotted in chondrite-normalized REE plots (Fig. 9). Plagioclase patterns are fractionated, with high LREE and low HREE contents and a conspicuous positive Eu anomaly for the andesite sample (Fig. 9a), as well as other notable positive anomalies for Ba and Sr (not shown). Orthopyroxene spectra are homogeneous, displaying low LREE relative to HREE contents, and a small negative Eu anomaly. Clinopyroxenes from the basaltic andesite sample display slightly flat spectra with maximum values for MREE and a small negative Eu anomaly (Fig. 9b). Lastly, two distinct populations of amphibole are identified (Fig. 9c): a REE-poor group that corresponds to amphibole from the basaltic andesite, and a REE-rich group that corresponds to the andesite and the rhyolite. These two populations are also observed for HFSE (e.g. Nb, Ta, Zr, not shown). Both groups display concave spectra with higher abundances of Nd (and other MREE) compared with other LREE and HREE. In addition, the REE-poor group corresponds to high-Al amphibole and display no Eu anomaly; whereas REE-rich group corresponds to high-Al amphibole and displays a conspicuous negative Eu anomaly. This feature indicated the contemporaneous crystallization of plagioclase, low-Al amphibole, orthopyroxene and clinopyroxene in the ADR group.

Figure 9

4.4. Chemical composition of interstitial matrix glass and melt inclusions

Interstitial matrix glass from the BA samples distributes into two compositional groups. Glasses from the *CE* 1667 eruptive products display homogeneous compositions (62.7-64.1 wt.% SiO_2; n=5, normalized to anhydrous values, Table 6), whereas those from the 2006-2009 and 2013-2017 samples show slightly more differentiated compositions (62.7-67.0 wt.% SiO_2, n=11). In contrast, interstitial glasses from whole-rock andesite samples from the 1-2 ka eruptions show dacitic to rhyolitic compositions (68.6-70.3 wt.% SiO_2; n=13), and glasses from whole-rock dacites and rhyolites samples display high-silica rhyolitic compositions (73.8-76.1 wt.% SiO_2; n=38). We analysed several melt inclusions from an andesitic and a rhyolitic tephra samples. We should stress the high homogeneity of these analyses that display almost similar compositions for both samples: 66.0 ± 1.4 wt.% SiO_2 (n=12) for MI in plagioclase crystals from andesitic tephra and 66.2 ± 1.2 wt.% SiO_2 (n=9) for MI in

plagioclase crystals from rhyolitic tephra. We should highlight that these compositions are identical to those of the interstitial matrix glasses from andesitic tephra. When plotted on Harker diagrams (Fig. 10), whole-rock, matrix glasses and melt inclusions samples define a single magmatic trend, although some scattering is observed for Al_2O_3 and Na_2O (not shown). Matrix glasses from the BA group fall outside this trend, especially for Al_2O_3 and K_2O. It is worth noting that the matrix glass from the andesite whole-rock samples displays an almost identical rhyolitic composition to the whole-rock rhyolites.

The water content of the matrix glasses was estimated using the "by difference" method (Devine et al., 1995). We stress that these values mostly correspond to degassed magmas and thus these values should be considered as rough minimum estimates of the pre-eruptive water content. Concerning the ADR samples, we found large glass shards that allowed us to perform defocused analyses to minimize Na migration. As a result, the water content of matrix glasses from the ADR samples is 4.0 ± 1.2 wt.% (n=51). In order to better constrain the pre-eruptive water content for ADR samples, we analysed plagioclase-hosted melt inclusions by Raman spectroscopy. The inclusions show variable water contents suggesting entrapment at different depths and/or complex degassing histories. The maximum value (6 wt.%) was measured in an inclusion of the rhyolitic tephra less affected by the magnetite signal (Supplementary material 3). Overall, minimum water contents of the melt inclusions from the andesitic samples range from 2.3 to 3 wt.%, whereas those from the rhyolitic samples span a range of 2.3 to 6 wt.% H_2O. Although most of the inclusions seem to be characterised by moderate water contents (2-3 wt.%), the true water contents are obtained only after correction for the underestimation caused by the presence of magnetite in the glass. The underestimate is proportional to the intensity of the magnetite peak and is evident in glasses with low (microprobe + Raman) totals (< 97 wt.%; Supplementary material 4). When this effect is taken into account and the compositions corrected, the water contents increase to varying degrees between 3 and 6 wt.%. Using the "by difference" method on MI analyses we obtain an average value of 5.6 ± 1.7 wt.% H_2O (n=21), in agreement with the results of Raman measurements.

Figure 10

Table 6

5. Discussion

5.1. Pre-eruptive P-T conditions

439   *ADR magmas.* Given that amphibole is ubiquitous in this magmatic group, a suitable geothermometer is based on

440   the amphibole-plagioclase equilibrium, using the edenite-richterite formulation of Holland and Blundy (1994),

441   which applies to quartz-free assemblages. We applied this geothermometer to euhedral amphibole-plagioclase

442   pairs in contact or for amphibole inclusions in plagioclase phenocrysts. We stress that this thermometer is weakly

443   affected by pressure changes (a change of 100 MPa induces a temperature difference of around 5 ºC). In Table 7,

444   the temperature estimates using the amphibole-plagioclase thermometer show a decrease in magmatic

445   temperatures from andesitic samples that yield very homogeneous values (913 ± 13 ºC, n=15), to dacites (881 ±

446   36 ºC, n=21), and rhyolites that show even lower values (846 ± 30 ºC, n=12).

447   Magnetite-ilmenite pairs are extremely rare in Ubinas magmatic series, however, we analysed 11 pairs

448   from dacites and rhyolites that follow the equilibrium criteria of Bacon and Hirschmann (1988). Using the Lindsley

449   and Spencer (1982) thermobarometric procedure, these pairs show very homogeneous T-fO_2 results. For dacites,

450   the magnetite-ilmenite thermometer yields a temperature of 879 ± 4ºC (n=9) and a fO_2 of -10.3 ± 0.1 (NNO+2);

451   whereas for rhyolites the temperature is slightly lower, 849 ± 3ºC (n=2) and fO_2 of -10.7 ± 0.1 (NNO+2). We

452   should stress the good agreement between these temperature estimates and those obtained from the amphibole-

453   plagioclase thermometer. However, as mentioned by Rutherford and Devine (1996), the magnetite-ilmenite

454   thermometer systematically displays higher values (up to 30ºC) for highly oxidized magmas (fO_2 between -10 and

455   -11). If we apply this empirical correction the estimated temperature should be ~850ºC for dacites and ~820ºC for

456   rhyolites.

457   Another reliable thermometer for this magmatic group is the plagioclase-melt formulation of Putirka

458   (2008). We applied this thermometer to mineral rims in equilibrium with the adjacent matrix glasses. We ensured

459   that equilibrium conditions had been attained by selecting euhedral crystals, and by comparing the plagioclase-

460   melt exchange coefficients with the putative values from the literature (K_d^{Ab-An} = 0.1 ± 0.05; Putirka, 2008). Given

461   that the pressure dependency on temperature estimates is negligible, we fixed a crystallisation pressure (see below)

462   in order to better constrain the magmatic temperature. We stress that a large pressure variation of around 500 MPa

463   induces a temperature variation within the method's error (Putirka, 2008). In contrast, a critical point with these

464   models concerns the pre-eruptive water content of magmas, because a change of 1 wt.% H_2O induces a variation

465   of ~20ºC (i.e. Putirka, 2008; Samaniego et al., 2011; Arpa et al., 2017). In this work, we consider water content of

466   6 wt.%, which corresponds to the maximum values measured in melt inclusions. In Table 7, we summarize

467   temperature estimates for the ADR group. As for the previous thermometers, the plagioclase-melt formulation

468   shows a decrease in magmatic temperatures from andesites (881 ± 5 ºC, n=6) to dacites and rhyolites that show

469   lower but similar values (787 ± 11 ºC, n=5 and 813 ± 5 ºC, n=8 respectively). We should stress these estimates are

470   systematically lower than those obtained by the other methods (Table 7).

471   Amphibole stability in calc-alkaline magmas has been widely used to estimate its crystallization pressure.

472   The Al-in-hornblende barometer has been experimentally calibrated for different ranges of temperature (Johnson

473   and Rutherford, 1989; Schmidt, 1992; Mutch et al., 2016). These formulations stipulate that the aluminium content

474   (Al^T) of amphibole is proportional to the crystallization pressure at specific conditions defined by a mineral

475   assemblage composed of plagioclase, sanidine, amphibole, biotite, quartz, sphene and Fe-Ti oxides. Given that

476   quartz is absent from the equilibrium assemblages at Ubinas, even from the rhyolitic magmas, this barometer

477   would yield anomalously high pressures. On the other hand, Ridolfi et al. (2010) and Ridolfi and Renzulli (2012)

478   looked again into amphibole stability in calc-alkaline magmas and proposed new empirical P-T-fO$_2$-XH$_2$O

479   formulations based on amphibole chemistry. However, many authors consider that Al^T in amphibole is sensitive

480   to both pressure and temperature variations (Poli and Schmidt, 1992; Anderson and Smith, 1995; Bachmann and

481   Dungan, 2002; Kiss et al., 2015). This implies that this barometer should be used within the specific temperature

482   range at which it was calibrated. In order to test the accuracy of these models, Erdmann et al. (2014) compared the

483   experimentally determined P-T conditions of a set of amphiboles with the values calculated using Ridolfi et al.

484   (2010) and Ridolfi and Renzulli (2012) formulations. Based on this analysis, Erdmann et al. (2014) concluded that

485   temperature estimates are acceptable, whereas pressure values are seriously flawed. Temperature estimates

486   obtained from the Ridolfi et al. (2010) and Ridolfi and Renzulli (2012) methods also show a decrease in magmatic

487   temperature from andesites to rhyolites groups (Table 7), although the absolute values are 30-60ºC higher than

488   those obtained with the magnetite-ilmenite, amphibole-plagioclase and plagioclase-melt thermometers. It is worth

489   noting that following Ridolfi and Renzulli (2002) method, for dacitic and rhyolitic magmas we obtain very similar

490   values for fO$_2$ that those obtained with the magnetite-ilmenite pairs (ΔNNO = 1.7 ± 0.3, n=45).

491   Pressure estimates are summarized in Table 7. We observe that most barometers show a progressive

492   decrease in amphibole crystallization pressure through the ADR samples. However, we should stress that the

493   temperature estimated for ADR group did not match those of the most common experimental calibrations (Johnson

494   and Rutherford, 1989; Schmidt, 1992; Mutch et al., 2016). For this reason, we focus on other calibrations that take

495   into account the influence of temperature on Al^T (Anderson and Smith, 1995) or by applying the formulation that

496   uses the ^{VI}Al for barometry (Médard and Le Pennec, 2013; Manrique et al., 2020). If we focus on amphibole

497   phenocryst of rhyolites and fixing the temperature at 820ºC (see above), we obtain 228 ± 86 MPa (n = 16) using

498   the temperature-corrected barometer of Anderson and Smith (1995). Using the temperature independent barometer

499   of Médard and Le Pennec (2013), we obtain rather higher values of 316 ± 51 MPa, which are indeed in the error

500   range of the methods. Other concordant results were obtained using the empirical barometers of Ridolfi et al.

501   (2010) and Ridolfi and Renzulli (2012), which yield similar values (237 ± 81 MPa and 252 ± 91 MPa,

502   respectively). In summary, it seems plausible that amphibole in silica-rich magmas (dacites and rhyolites)

503   crystallized at 200-400 MPa (Fig. 11) and temperatures in the range of 800-850ºC.

504

505   ***BA magmas.*** Given the presence of ortho- and clinopyroxene in BA and andesitic magmas, a suitable

506   geothermometer is the two-pyroxene thermometer (*cf.* Lindsley, 1983). Rivera et al. (2014) applied this

507   thermometer for the 2006-2009 magmas and obtained temperatures of 950-1020ºC (n=6). A careful observation

508   of these orthopyroxene-clinopyroxene pairs reveals that most of them do not follow the equilibrium criteria defined

509   by the comparison of the calculated exchange coefficients with the putative values from the literature (K_d^{Fe-Mg} =

510   1.09 ± 0.14; Putirka, 2008). This analysis shows that only two orthopyroxene-clinopyroxene pairs from Rivera el

511   al. (2014), one pair from our dataset and five additional pairs from older samples of older Ubinas samples (Rivera,

512   2010) follow the equilibrium criteria. These pairs yield a temperature of 993 ± 24 (n=8) for BA samples. This

513   value is very close to the temperatures obtained with the amphibole-based Ridolfi et al. (2010) method (994 ± 9ºC,

514   n=23).

515   Given that most barometers are not calibrated for basaltic andesitic compositions, that the mineral

516   assemblage of these magmas do not meet those needed for the method, and that the temperatures obtained for the

517   BA group are far from the calibration temperatures of most barometers, the pressure estimates for this group are

518   much more difficult to compute. In addition, we observe that the temperature-controlled edenite substitution is

519   much more important than the pressure-controlled tschermakite substitution (Fig. 8), which implies that the

520   differences in amphibole chemistry are mostly related to temperature, with a minor role for pressure and magma

521   chemistry. The empirical barometers of Ridolfi et al. (2010) and Ridolfi and Renzulli (2012) yield pressures of

522   453 ± 26 MPa and 357 ± 138 (n = 23) respectively, whereas the temperature-independent barometer of Médard

523   and Le Pennec (2013) yields values of 341 ± 35 MPa (i.e. no difference between amphiboles from ADR and BA

524   groups, Fig. 11). Given the uncertainties associated with the application of these models to the BA magmas, we

525   conclude that these amphiboles probably crystallized at higher pressure (>300-400 MPa) and temperatures (1000-

526   1050ºC).

527

528   Figure 11

529   Table 7

530

531   **5.2. The origin of the magmatic diversity: trans-crustal assimilation and fractional crystallization**

532   **processes**

533   The magmatic differentiation in continental arc settings is a complex process including fractional

534   crystallization coupled with crustal assimilation at several levels in the crust. In addition, frequent recharge and

535   the subsequent magma mixing process is ubiquitous of active magmatic systems. We should stress that these

536   processes are not mutually exclusive, acting at the same time during magma ascent and storage across the crust.

537   Given that the Andean Central Volcanic Zone developed on a thick (up to 70 km) continental crust, it represents

538   the archetype for studying the crustal participation on continental arc magmatism. Most studies consider these

539   magmas stagnate at different levels in the crust and acquire its geochemical signature at the so-called MASH

540   (Melting-Assimilation-Storage-Homogenization) zones located in the deep and hot lower crust (Hildreth and

541   Moorbath, 1988; Davidson et al., 1990; Muir et al., 2014). Then, intermediate magmas could stagnate again at

542   shallow levels, where they differentiate via a coupled assimilation-fractional crystallization process. More

543   recently, Blum-Oeste and Wörner (2016) identified three different geochemical end-members able to explain the

544   whole variability of CVZ magmas: (1) a slightly evolved calc-alkaline basaltic andesite; (2) an enriched

545   shoshonitic basalt; and, (3) a crustal-derived rhyodacite. These authors propose that all CVZ magmas derived from

546   mixing process at variable proportions of these three end-members.

547   The Ubinas magmatic series, which is composed of basaltic andesites through to rhyolites, has been

548   interpreted as a result of a coupled assimilation and fractional crystallization process occurring at different depth

549   in the crust (Thouret et al., 2005; Rivera, 2010). These authors also suggest that the mafic magmas resulted of a

550   deep crustal differentiation process involving amphibole and/or garnet. Our geochemical data shows a conspicuous

551   break-in-slope observed at 56-57 wt.% SiO_2 in compatible elements (MgO, Ni, Sr, Fig. 4). This feature indicates

552   the early crystallization of an olivine-dominated cumulate in BA magmas, followed by the fractionation of

553   clinopyroxene, amphibole and plagioclase for ADR magmas. In addition, the frequent zoning patterns observed

554   in plagioclase and pyroxenes; and, the fact that the matrix glass compositions fall on the main Ubinas geochemical

555   trend (Fig. 10), corroborates the progressive fractionation process.

556   Experimental data on crystallization of primitive arc magmas at mid- to lower-crustal pressures show a

557   continuous geochemical trend from primitive magnesian basalts up to high-silica rhyolites (Müntener et al., 2001;

558   Sisson et al., 2005; Pichavant and Macdonald, 2007; Alonso-Perez et al., 2009; Blatter et al., 2013; Nandedkar et

559   al., 2014). These experiments were performed from near-liquidus temperatures (~1150-1200ºC) down to

560   temperatures as low as 700ºC; pressures ranging from 900 to 400 MPa; and at oxidizing (NNO+2) and moderately

561   hydrous (~3-4 wt.% H_2O) conditions. At high pressure and temperature (900-700 MPa; 1200-950ºC), the dominant

562   crystallizing minerals are clinopyroxene + olivine + Cr-Spinel ± orthopyroxene. At lower pressure and

563   temperature, plagioclase begins to crystallize, Fe-Ti oxides replaces spinel, olivine dissolves and amphibole

564   crystallization begins (at temperatures below ~1000ºC). At the end of the crystallization sequence, apatite, quartz

565   and biotite appear as liquidus phases. In Fig. 10 we compare the major element compositions of the whole-rock

566   and matrix glasses and melt inclusions from Ubinas with fields of selected experimentally-determined liquids

567   (Sisson et al., 2005; Blatter et al., 2013; Nandedkar et al., 2014). We observe a reasonable correspondence, except

568   for the mafic compositions (> 5 wt.% MgO), which are lacking in the Ubinas magmatic series, and globally lower

569   values of K_2O (not shown), related to the composition of the starting material. These results imply that the

570   commonly observed mineral assemblage in Ubinas samples records a long crystallization sequence, roughly

571   spanning from 900 to 200 MPa, and from 1150 to 700ºC.

572   Additional constraints on magmatic differentiation come from trace elements systematics. The negative

573   correlation of Sr with silica increase suggest a significant role of plagioclase, whereas the decrease of the transition

574   metals (e.g. Ni, Sc, V) suggest the fractionation of clinopyroxene and olivine, namely for BA group. In addition,

575   trace element systematics supports the leading role of amphibole fractionation for the ADR group. On the basis of

576   theoretical and experimental studies, amphibole preferentially incorporates MREE over HREE and LREE (*cf.*

577   Davidson et al., 2007). This observation is corroborated by the Ubinas amphibole trace element patterns (Fig. 9),

578   which show that fractionation of this mineral leads to an increase in La/Nd and a decrease in Nd/Yb and Dy/Yb

579   with silica contents in the magma (Fig. 12a, b). In order to test the hypothesis of an amphibole-controlled fractional

580   crystallization process, we performed a two-steps geochemical modelling procedure. First, major element mass-

581   balance calculations (Bryan et al., 1969) between mafic and felsic end-members (e.g. UBI-10-18C and UBI-10-

582   11, respectively) allow us to estimate the modal composition of the cumulate (46–48% Pl + 38–44% Amph + 3–

583   5% Cpx + 6% Mag + 1% Apt), as well as the degree of fractionation (50-55%) required to evolve from a BA to a

584   ryholitic end-members. It is worth noting that the modal composition of the cumulate estimated by mass-balance

585   is coherent with the observed mineral assemblage of Ubinas samples and confirms the leading role of amphibole

586   fractionation. Then, these results were used in the trace element modelling of a Rayleigh-type fractional

587   crystallization (FC), using partition coefficients for intermediate liquids (Rollinson, 1993; Bachmann et al. 2005;

588   Rivera et al., 2017). We also observe that isotopic ratios are correlated with silica as well as with some trace

elements ratios (e.g. Dy/Yb, Fig. 12c, d), and that the higher values for both parameters (i.e. Dy/Yb and $^{143}Nd/^{144}Nd$) roughly correspond to the BA samples. Consequently, a pure fractional crystallization processes cannot explain these variations: the changes in isotopic ratios clearly point at of some degree of crustal assimilation. Based on this observation, we performed an assimilation-fractional crystallization (AFC, DePaolo, 1981) model, using exactly the same parameters than for the FC model, with different fractionation/assimilation ratios (r = 0.04-0.10) and using the local upper continental crust represented by the Precambrian Charcani gneiss (Boily et al., 1990; Rivera et al., 2017) as a potential contaminant. The modelling results for both FC and AFC models are shown in Fig. 13. These models show a good agreement for most trace elements in the multi-parameter plot (Fig. 13a), as well as in the binary plots including key trace elements ratios and isotopic rapports (Fig. 13b, c), although a mismatch is observed for some trace elements as the LREE. These models suggest a proportion of assimilated crust of 2-6 vol.% (following the procedure of Aitcheson and Forrest, 1994).

Lastly given that Sr-Nd-Pb ratios plot far beyond the mantle values, with only weak isotopic variations between the basaltic andesitic and rhyolitic end-members (with a silica variation of more than 15 wt.%), we suggest that the isotopic signature of BA Ubinas magmas was mostly acquired at a deep stage of magmatic differentiation, probably in the lower crust MASH zone. Single mass-balance models confirm that 20-30% of a putative lower crust is needed to shift the mantle-derived magmas to those of the BA Ubinas samples. Given the large uncertainties concerning the deep fractionation processes as well as the lower crustal compositions, we did not perform a quantitative analyse of these deep processes. However, this two-steps model has been applied on a regional Andean scale (Hildreth and Moorbath, 1988; Mamani et al., 2010; Blum-Oeste and Wörner, 2016; Ancellin et al., 2017) as well as to specific volcanic centres such as the Andahua monogenetic cones (Delacour et al., 2007), El Misti (Rivera et al., 2017), Ollagüe (Feeley and Davidson, 1994; Matioli et al., 2006), Nevados de Payachata (Davidson et al., 1990), and Lascar (Sainlot et al., 2020) in the CVZ; and Cotopaxi (Garrison et al., 2011) and Tungurahua volcanoes (Nauret et al., 2018) in the NVZ.

Figure 12

Figure 13

5.3. The magmatic plumbing system and the progressive temporal changes in magma chemistry

The geochemical data for the Ubinas magmatic series reveals a large compositional variation that could be explained by a coupled assimilation-fractional crystallization (AFC) process involving a mineral assemblage

composed of plagioclase, amphibole, orthopyroxene, clinopyroxene, Fe-Ti oxides, with minor olivine and biotite (at the mafic and felsic end-members respectively). A key geochemical characteristic of the Ubinas magmatic series is the overall variation of most geochemical parameters. As discussed above, Ubinas magmas become less differentiated through time (Fig. 3, 4, Supplementary materials 5 and 6), with the recently erupted magmas (the BA group) displaying the highest $^{143}Nd/^{144}Nd$ and lowest $^{87}Sr/^{86}Sr$ isotopes (Fig. 5, Supplementary materials 6), indicating that BA magmas are among the most primitive compositions erupted during the last millennium. In addition, as demonstrated by Rivera et al. (2014) for the 2006-2009 eruptions, and corroborated by 2013-2017 magmas (this work), the BA magmas display frequent disequilibrium textures, such as inversely zoned plagioclase phenocrysts with sieve textures and overgrowth rims, inversely zoned clinopyroxene phenocrysts, and rare olivine crystals with reaction and overgrowth rims. These features point to a magma mixing scenario between two magmas of similar basaltic andesitic compositions but different temperature and volatile contents (Rivera et al., 2014). Thus, we infer that during the historical and recent eruptions the trans-crustal magmatic reservoir was fed by mafic magmas at depth. In contrast, it is worth noting that disequilibrium textures and other magma mixing evidences (e.g. banded samples) are absent in the ADR samples. However, we should stress that mixing of hybrid magmas of different degrees of differentiation is a ubiquitous process at the trans-crustal magmatic systems.

Due to the thick continental crust, primitive basaltic magmas are extremely rare in the Central Andes, with notable exceptions, for example the Andahua monogenetic cones in Southern Peru (Delacour et al., 2007; Sørensen and Holm, 2008). On the whole, the primitive Central Andes magmas display variably enriched trace element patterns as well as variable radiogenic isotopic signatures (Mamani et al., 2010; Blum-Oeste and Wörner, 2016), which must have been acquired at the so-called lower-crustal hot zones (Hildreth and Moorbath, 1988; Annen et al., 2006). During their ascent from the lower crust, these magmas stall at different levels in the thick Central Andes crust and then feed the middle-to-upper crustal magma system.

On the basis of the petrological data presented in this work, we are able to reconstruct the upper part of the magma plumbing system over the last millennia. Although most barometers indicate two distinct pressure populations for ADR and BA magmas, we cannot confirm these differences due to the fact that most magmas (namely the BA group) do not meet neither the mineralogical assemblage nor the temperature range stipulated for the models. If we focus on most differentiated magmas of Ubinas series (dacites and rhyolites), and taking into account the intrinsic uncertainties related with the methods, we consider that amphibole from these magmas crystallized in the range of 200-400 MPa, which is realistic for dacitic and rhyolitic magmas in arc settings (Rutherford and Hill, 1993; Moore and Carmichael, 1998; Martel et al., 1999; Scaillet and Evans, 1999; Rutherford

and Devine, 2003; Andujar et al., 2017; Martel et al., 2018). Considering a bulk density value for upper crustal rocks of 2600 kg/m^3, and the pressure-depth relationship of Blundy and Cashman (2008), the ADR magma storage region would be located at 8-15 km below the summit. We imagine this magma storage region as a plexus of sill-like intrusions that conform a mushy magma reservoir (cf. Annen et al., 2006; Wörner et al., 2018). This reservoir should be frequently fed by primitive BA magmas that certainly formed deeper in the crust as a result of AFC process from primitive arc magmas, as suggested by phase-equilibrium studies revealing that primitive arc magmas in arc settings stall and differentiate at even higher pressures (up to 900 MPa, 30-35 km deep; Blatter et al., 2013; Nandedkar et al., 2014).

During Holocene times, the Ubinas magma plumbing system stored a large amount of differentiated (andesitic to rhyolitic) magmas. As a result, Ubinas experienced notable plinian eruptions, the last one occurred at 1-2 ka. In contrast, over the last few centuries, Ubinas experienced smaller eruptions involving BA magmas. Although we cannot exclude a bias due to the fact that smaller basaltic andesitic events might not be preserved in the geological record, it seems clear that the current state of the Ubinas magma plumbing system corresponds to a phase of recharge, with no evidence for a rejuvenation of the silica-rich reservoir that fed the large Holocene dacitic to rhyolitic eruptions. This conclusion is corroborated by recent seismological studies showing that volcano-tectonic events at Ubinas are clustered below the summit caldera and up to 8 km depth (Inza et al., 2014; Gonzalez et al., 2014; Machacca-Puma et al., 2019). In addition, some regional geophysical studies in this part of the Andes have not identified low velocity anomalies that could be interpreted as a large magma storage zone, suggesting a reservoir of relatively modest dimensions that is unable to be imaged by the spatial resolution of the regional tomographic studies (*cf.* Ryant et al., 2016).

Figure 14

6. Conclusions

During the last millennia (i.e. post-glacial and Holocene times) and recently, the eruptive products of Ubinas have shown an overall decrease in silica content from the older rhyolites (69-71 wt.% SiO$_2$) to the historical and recent basaltic andesites (55-57 wt.% SiO$_2$). K$_2$O and certain incompatible trace elements (e.g. Rb, Th) are positively correlated with silica; whereas MgO concentration, as well the compatible elements (e.g. Sr, Y, Yb, Ni, Cr) display an overall increase from the older rhyolites to the younger basaltic andesites, peaking in the *CE* 1667 eruption products. In contrast to these large major and trace element variations, Sr-Nd-Pb isotopic values show

679 generally highly radiogenic values but little variation from basaltic andesites to rhyolites. We note that the isotopic

680 data indicate that magmas erupted during the recent eruptions of Ubinas rank amongst the most primitive magmas

681 erupted by this volcano during the last millennia. These temporal patterns indicate that the Ubinas magmatic series

682 evolved in the middle-to-upper crust by a coupled Assimilation-Fractional Crystallization (AFC) process involving

683 a cumulate composed of plagioclase, amphibole, clinopyroxene, orthopyroxene and Fe-Ti oxides with minor

684 amounts of olivine and biotite at the mafic and felsic end-members. The role of upper crustal assimilation is limited

685 and constrained to maximum a few per cent; however, the highly radiogenic Sr-Nd-Pb signature of Ubinas magmas

686 requires a higher degree of crustal processing, which must have occurred at lower crustal depths.

687 The detailed petrological study of the Ubinas magmatic series points to an overall variation in P-T

688 conditions, from the older and colder dacites and rhyolites up to the younger (historical and recent), hotter and

689 probably deeper basaltic andesites. These data, together with geochemical and phase equilibrium constraints allow

690 us to propose the existence of an elongated upper crust magma reservoir composed of a highly crystalline mush

691 with some batches of liquid magma. Our study reveals that the large Holocene andesite-dacite-rhyolite (ADR)

692 eruptions require the existence of a large shallower reservoir at 200-400 MPa, which seems to be recharged by the

693 historical and recent (*CE* 1667, 2006-2009, 2013-2017) basaltic andesitic magmas, which were formed at deeper

694 levels in the crust. This study highlights the importance of detailed petrological studies of Holocene sequences at

695 explosive arc volcanoes in order to constrain the magmatic processes and conditions that control the occurrence

696 of large explosive eruptions.

697

705

706 **References**

707 Aitcheson, S.J., Forrest, A.H., 1994. Quantification of crustal contamination in open magmatic systems. Journal

708   of Petrology 35, 461–488.

709   Alonso-Perez, R., Muntener, O., Ulmer. P., 2009. Igneous garnet and amphibole fractionation in the roots of island

710   arcs: experimental constraints on andesitic liquids. Contrib. Mineral. Petrol. 157,541–558.

711   Ancellin, M.A., Samaniego, P., Vlastélic, I., Nauret, F., Gannoun, M., Hidalgo, S., 2017. Across-arc versus along-

712   arc Sr-Nd-Pb isotope variations in the Ecuadorian volcanic arc. Geochem. Geophys. Geosyst. 18, 1163–1188.

713   Anderson, J.L., Smith, D.R., 1995. The effects of temperature and fO_2 on the Al-in-hornblende barometer. Am.

714   Mineral. 80, 549-559.

715   Andujar, J., Martel, C., Pichavant, M., Samaniego, P., Scaillet, B., Molina, I., 2017. Structure of the plumbing

716   system at Tungurahua volcano, Ecuador: Insights from phase equilibrium experiments on July-August 2006

717   eruption products. J. Petrol. 58, 1249-1278.

718   Annen, C., Blundy, J.D., Sparks, R.S.J., 2006. The genesis of intermediate and silicic magmas in deep crustal hot

719   zones. J. Petrol. 47, 505-539.

720   Arpa, M.C., Zellmer, G.F., Christenson, B., Lube, G., Shellnutt, G., 2017. Variable magma reservoir depths for

721   Tongariro Volcanic Complex eruptive deposits from 10,000 years to present. Bull. Volcanol, 79, 56. http://doi

722   10.1007/s00445-017-1137-5

723   Bachmann, O., Dungan, M.A., 2002. Temperature- induced Al-zoning in horblendes of the Fish Canyon magma,

724   Colorado. Am. Mineral. 87, 723-738.

725   Bachmann, O., Huber, C., 2016. Silicic magma reservoirs in the Earth's crust. Am. Mineral. 101, 2377-2404.

726   Blard., P.H., Lave, J., Farley, K.A., Ramirez, V., Jimenez, N., Martin, L., Charreau, J., Tibari, B., Fornari, M.,

727   2014. Progressive glacial retreat in the Southern Altiplano (Uturuncu volcano, 22º S) between 65 and 14 ka

728   constrained by cosmogenic ^{3}He dating. Quat. Res. 82, 209-221.

729   Blatter, D.L., Sisson, T.W., Hankins, W.B., 2013. Crystallization of oxidized, moderately hydrous arc basalt at

730   mid- to lower-crustal pressures: Implications for andesite genesis. Contrib. Mineral. Petrol. 166, 861-886.

731   Blum-Oeste, M., Wörner, G., 2016. Central Andean magmatism can be constrained by three ubiquitous end-

732   members. Terra Nova 28, 434-440.

733   Blundy, J.D., Cashman, K.V., 2008. Petrologic reconstruction of magmatic system variables and processes. Rev.

734   Mineral. Geochem. 69, 197–239.

735   Boily, M., Ludden, J.N., Brooks, C., 1990. Geochemical constraints on the magmatic evolution of the pre- and

736   post-Oligocene volcanic suites of southern Peru: implication for the tectonic evolution of the central volcanic

737   zone. Geological Society of America Bulletin 102, 1565–1579.

738   Bromley, G.R.M., Schaefer, J.M., Wincler, G., Hall, B.L., Todd, C.E., Rademaker, C.K.M., 2009. Relative timing

739   of last glacial maximum and late-glacial events in the central tropical Andes. Quat. Sci. Rev. 28, 2514–2526.

740   Cashman, K.V., Sparks, R.S.J., Blundy, J.D., 2016. Vertically extensive and unstable magmatic systems: A unified

741   view of igneous processes. Science 355, eaag3055.

742   Cotten, J., Le Dez, A., Bau, M., Caroff, M., Maury, R.C., Dulski, P., Fourcade, S., Bohn, M., Brousse, R., 1995.

743   Origin of anomalous rare-earth element and Yttrium enrichments in subaerial exposed basalts: evidence from

744   French Polynesia. Chem. Geol. 119, 115–138.

745   Davidson, J.P., Harmon, R.S., Wörner, G., 1991. The source of the Central Andes magmas; some considerations.

746   Andean Magmatism and Its Tectonic Setting. Geological Society of America, Special Paper 265, 233–243.

747   Davidson, J.P., Turner, S., Handley, H., Macpherson, C., Dosseto, A., 2007. Amphibole "sponge" in arc crust?

748   Geology 35, 787-790.

749   De Angelis, S.H., Larsen, J., Coombs, M., 2013. Pre-eruptive magmatic conditions at Augustine volcano, Alaska,

750   2006: Evidence from amphibole geochemistry and textures. Journal of Petrology 54, 1939-1961.

751   Delacour, A., Gerbe, M.C., Thouret, J.C., Wörner, G., Paquereau, P., 2007. Magma evolution of Quaternary minor

752   volcanic centres in Southern Peru, Central Andes. Bulletin of Volcanology 69, 581-608.

753   Devine, J.D., Gardner, J.E., Brack, H.P., Layne, G.D., Rutherford, M.J., 1995. Comparison of microanalytical

754   methods for estimating H_2O contents of silicic volcanic glasses, Am. Mineral. 80, 319-328.

755   Deer, W.A., Howie, R.A., Zussman J., 2013. An introduction to the rock-forming minerals. 3rd edition. The

756   Mineralogical Society, London, 498 pp.

757   Di Genova, D., Sicola, S., Romano, C., Vona, A., Fanara, S., Spina, L., 2017. Effect of iron and nanolites on

758   Raman spectra of volcanic glasses: a reassessment of existing strategies to estimate the water content. Chem.

759   Geol. 475, 76–86.

760   Eichelberger, J.C., Izbekov, P.E., Browne, B.L., 2006. Bulk chemical trends at arc volcanoes are not liquid lines

761   of descent. Lithos 87, 135–154.

762   Erdmann, S., Martel, C., Pichavant, M., Kushnir, A., 2014. Amphibole as an archivist of magmatic crystallization

763   conditions: problems, potential, and implications for inferring magma storage prior to the paroxysmal 2010

764   eruption of Mount Merapi, Indonesia. Contrib. Mineral. Petrol. 167, 1016.

765   Feeley, T.C., Davidson, J.P., 1994. Petrology of calc-alkaline lavas at Volcan Ollagüe and the origin of

766   compositional diversity at Central Andean stratovolcanoes. J. Petrol, 3, 1295–1340

767   Galer, S.J.G., Abouchami, W., 1998. Practical application of lead triple spiking for correction of instrumental mass

768   discrimination. Mineral. Mag. 62A, 491–492.

769   Garrison, J.M., Davidson, J.P., Hall, M.L., Mothes, P., 2011. Geochemistry and petrology of the most recent

770   deposits from Cotopaxi Volcano, Northern Volcanic Zone, Ecuador. J. Petrol. 52, 1641–1678.

771   Gonzalez, K., Finizola, A., Lénat, J.F., Macedo, O., Ramos, D., Thouret, J.C., Fournier, N., Cruz, V., Pistre, K.,

772   2013. Asymmetrical structure, hydrothermal system and edifice stability: The case of Ubinas volcano, Peru,

773   revealed by geophysical surveys. J. Volcanol. Geoth. Res. 276, 132–144.

774   Grove, T.L., Elkins-Tanton, L.T., Parman, S.W., Chatterjee, N., Muntener, O., Gaetani, G.A., 2003. Fractional

775   crystallization and mantle-melting controls on calc-alkaline differentiation trends. Contrib. Mineral. Petrol.

776   145, 515-533.

777   Hildreth, W., Moorbath, S., 1988. Crustal contributions to arc magmatism in the Andes of central Chile. Contrib.

778   Mineral. Petrol. 98, 455–489.

779   Holland, T., Blundy, J., 1994. Non-ideal interactions in calcic amphiboles and their bearing on amphibole-

780   plagioclase thermometry. Contrib. Mineral. Petrol. 116, 433–447.

781   Inza, L.A., Metaxian, J.P., Mars, J.I., Bean, C.J., O'Brien, G.S., Macedo, O., Zandomeneghi, D., 2014. Analysis

782   of dynamics of vulcanian activity of Ubinas volcano, using multicomponent seismic antennas. J. Volcanol.

783   Geotherm. Res, 270, 35–52.

784   Jackson, M.C., Blundy, J., Sparks, R.S.L., 2018. Chemical differentiation, cold storage and remobilization of

785   magma in the Earth's crust. Nature 564. 405-409.

786   Johnson, M.C., Rutherford, M.J., 1989. Experimental calibration of the aluminum-in-hornblende geobarometer

787   with application to Long Valley caldera (California) volcanic rocks. Geology 17, 837-841.

788   Juvigné, E., Thouret, J.C., Gilot, E., Gourgaud, A., Legros, F., Uribe, M., Graf, K., 1997. Etude

789   tephrostratigraphique et bioclimatique du Tardiglaciaire et de l'Holocène de la Laguna Salinas, Pérou

790   méridional. Géographie physique et Quaternaire 51, 219–231.

791   Kelemen, P.B., Hanghøj, K., Greene, A.R., 2014. One view of the geochemistry of sub- duction-related magmatic

792   arcs, with an emphasis on primitive andesite and lower crust. A2 – Holland, Heinrich, D. In: Turekian, K.K.

793   (Ed.), Treatise on Geochemistry, Second Edition, Elsevier, Oxford, pp. 749–806

794   Kent, A., Darr, C., Koleszar, A., Salisbury, M., Cooper, K., 2010. Preferential eruption of andesitic magmas

795   through recharge filtering. Nat Geosci 3, 631–636.

796   Kiss, B., Harangi, S., Ntaflos, T., Mason, P.R.D., Pál-Molnár, E., 2014. Amphibole perspective to unravel pre-
797   eruptive processes and conditions in volcanic plumbing systems beneath intermediate arc volcanoes: a case
798   study from Ciomadul volcano (SE Carpathians). Contrib. Mineral. Petrol. 167, 986.

799   Krawczynski, M., Grove, T., Behrens, H., 2012. Amphibole stability in primitive arc magmas: effects of
800   temperature, H2O content, and oxygen fugacity. Contrib. Mineral. Petrol. 164, 317–339.

801   Leake, B.E., Woolley, A.R., Arps, C.E.S., Birch, W.D., Gilbert, M.C., Grice, J.D., Hawthorne, F.C., Kato, A.,
802   Kisch, H.J., Krivovichev, V.G., Linthout, K., Laird, J., Mandarino, J.A., Maresch, W.V., Nickel, E.H., Rock,
803   N.M.S., Schumacher. J.C., Smith. D.C., Stephenson, C.N., Ungaretti, L., Whittaker, E.J.W., Youzhi, G., 1997.
804   Nomenclature of amphiboles: report of the Subcommittee on Amphiboles of the International Mineralogical
805   Association, commission on new minerals and minerals' names. Am. Miner. 82, 1019–1037.

806   Lee, C.T.A., Bachmann, O., 2014. How important is the role of crystal fractionation in making intermediate
807   magmas? Insights from Zr and P systematics. Earth Planet. Sci. Lett. 393, 266-274.

808   Lindsley, D.H., 1983. Pyroxene thermometry. Am. Mineral. 68, 477–493.

809   Luhr, J.F., Carmichael, I.S.E., 1990. Petrological monitoring of cyclical eruptive activity at Volcán Colima,
810   Mexico. J. Volcanol. Geotherm. Res. 42, 235–260.

811   Machacca-Puma, R., Lesage, P., Larose, E., Lacroix, P., Anccasi-Figueroa, R.M., 2019. Detection of pre-eruptive
812   seismic velocity variations at an andesitic volcano using ambient noise correlation on 3-component stations:
813   Ubinas volcano, Peru. J. Volcanol. Geotherm. Res. 381, 83–100.

814   Mamani, M., Wörner, G., Sempere, T., 2010. Geochemical variation in igneous rocks of the Central Andean
815   orocline (13 °S to 18 °S): tracing crustal thickening and magmas generation through time and space. Geological
816   Society of America Bulletin 97, 241–254.

817   Manrique, N., Samaniego, P., Médard, E., Schiavi, F., Mariño, J., Liorzou, C., 2020. Pre-eruptive magmatic
818   processes associated with the historical (218 ± 14 aBP) explosive eruption of Tutupaca volcano (southern
819   Peru). Bull. Volcanol. 82, 6.

820   Martel, C., Pichavant, M., Holtz, F., Scaillet, B., Bourdier, J.L, Traineau, H., 1999. Effects of fO_2 and H_2O on
821   andesite phase relations between 2 and 4 kbar. J. Geophys. Res. 104, 29453–29470.

822   Martel, C., Andújar, J., Mothes, P., Scaillet, B., Pichavant, M., Molina, I., 2018. Storage conditions of the mafic
823   and silicic magmas at Cotopaxi, Ecuador. J. Volcanol. Geotherm. Res. 354, 74-86.

824   Matioli, M., Renzulli, A., Menna, M., Holm, P.M., 2006. Rapid ascent and contamination of magmas through the

825   thick crust of the CVZ (Andes, Ollagüe region): Evidence from a nearly aphyric high-K andesite with skeletal

826   olivines. J. Volcanol. Geotherm. Res. 158, 87-108.

827   Médard, E., Le Pennec, J.L., Francomme, J.E., Temel, A., Nauret, F., 2013. Reconstructing the magma feeding

828   system of the Cappadocian ignimbrites (Turkey) through amphibole thermobarometry. Goldschmidt

829   conference, Florence.

830   Moore, G., Carmichael, I.S.E., 1998. The hydrous phase equilibria (to 3 kbar) of an andesite and basaltic andesite

831   from western Mexico: constraints on water content and conditions of phenocryst growth. Contrib. Mineral.

832   Petrol. 130, 304–319.

833   Morimoto, N., Fabries, J., Ferguson, A.K., Ginzburg, I.V., Ross, M., Seifert, F.A., Zussman, J., 1988.

834   Nomenclature of pyroxenes. Am. Miner. 73, 1123-1133.

835   Muir, D., Blundy, J.D., Hutchinson, M.C. Rust, A.C., 2014. Petrological imaging of an active pluton beneath Cerro

836   Uturuncu, Bolivia. Contrib. Mineral. Petrol. 167, 980.

837   Müntener, O., Kelemen, P., Grove, T.L., 2001. The role of H_2O during crystallization of primitive arc magmas

838   under uppermost mantle conditions and genesis of igneous pyroxenites: an experimental study. Contrib.

839   Mineral. Petrol. 141, 643–658.

840   Mutch, E.J.F., Blundy, J.D., Tattitch, B.C., Cooper, F.J., Brooker, R.A., 2016. An experimental study of amphibole

841   stability in low-pressure granitic magmas and a revised Al-in-hornblende geobarometer. Contrib. Mineral.

842   Petrol. 171, 85.

843   Nandedkar, R.H., Ulmer, P., Müntener, O., 2014. Fractional crystallization of primitive, hydrous arc magmas: an

844   experimental study at 0.7 GPa. Contrib. Miner. Petrol. 167, 1015.

845   Nauret, F., Samaniego, P., Ancellin, M.A., Tournigand, P.Y., Le Pennec, J.L., Vlastélic, I., Gannoun, A., Hidalgo,

846   S., Schiano, P., 2018. The genetic relationship between andesites and dacites at Tungurahua volcano, Ecuador.

847   J. Volcanol. Geotherm. Res. 349, 283-297.

848   Peccerillo, P., Taylor, S.R., 1976. Geochemistry of Eocene calc-alkaline volcanic rocks from the Kastamonu area,

849   northern Turkey. Contrib. Mineral. Petrol. 58, 63–81.

850   Pichavant, M., Macdonald, R., 2007. Crystallization of primitive basaltic magmas at crustal pressures and genesis

851   of the calc-alkaline igneous suite: experimental evidence from St Vincent, Lesser Antilles arc. Contrib.

852   Mineral. Petrol. 154, 535–558.

853   Pin, C., Briot, D., Bassin, C., Poitrasson, F., 1994. Concomitant separation of strontium and samarium-neodymium

854   for isotopic analysis in silicate samples, based on specific extraction chromatography. Anal. Chim. Acta 298,

855   209–214.

856   Pin, C., Santos Zalduegui. J.F., 1997. Sequential separation of light rare- earth elements, thorium and uranium by

857   miniaturized extraction chromatography: application to isotopic analyses of silicate rocks. Anal. .Chim. Acta

858   339, 79–89.

859   Poli, S., Schmidt, M.W., 1992. A comment on Calcic amphibole equilibria and a new amphibole-plagioclase

860   thermometrer by J.D. Blundy and T.J.B. Holland. Contrib. Mineral. Petrol. 104, 208-224.

861   Prouteau, G., Scaillet, B., 2003. Experimental constraints on the origin of the 1991 Pinatubo dacite. Journal of

862   Petrology 44, 2203–2241.

863   Putirka, K.D., 2008. Thermometers and barometers for volcanic systems. Rev. Mineral. Geochem. 69, 61–111.

864   Putirka, K.D., 2016. Amphibole thermometers and barometers for igneous systems and some implications for

865   eruption mechanisms of felsic magmas at arc volcanoes. Am. Mineral. 101, 841-858.

866   Rawson, H., Keller, T., Fontijn, K., Pyle, D.M., Mather, T.A., Smith, V.C., Naranjo, J.A., 2016. Compositional

867   variability in mafic arc magmas over short spatial and temporal scales: evidence for the signature of mantle

868   reactive melt channels. Earth Planet, Sci. Lett. 456, 66–77.

869   Reubi, O., Blundy, J., 2009. A dearth of intermediate melts at subduction zone volcanoes and the petrogenesis of

870   arc andesites. Nature 461, 1269–1273.

871   Ridolfi, F., Renzulli, A., Puerini, M., 2010. Stability and chemical equilibrium of amphibole in calc-alkaline

872   magmas: an overview, new thermobarometric formulations and application to subduc- tion-related volcanoes.

873   Contrib. Mineral. Petrol. 160, 45–66.

874   Ridolfi, F., Renzulli, A., 2012. Calcic amphiboles in calc-alkaline and alkaline magmas: thermobarometric and

875   chemometric empirical equations valid up to 1130ºC and 2.2 GPa. Contrib. Mineral. Petrol. 163, 877–895.,

876   Rivera, M., 2010. Genèse et évolution des magmas andésitiques à rhyodacitiques récents des volcans Misti et

877   Ubinas (Sud du Pérou). Unpublished PhD thesis, Université Blaise Pascal, Clermont-Ferrand, France, 407 pp

878   Rivera, M., Thouret, J.C., Mariño, J., Berolatti, R., Fuentes, J., 2010. Characteristics and management of the 2006–

879   2008 volcanic crisis at the Ubinas volcano (Peru). J. Volcanol. Geotherm. Res. 198, 19–34.

880   Rivera, M., Thouret, J.C., Samaniego, P., Le Pennec, J.L., 2014. The 2006–2009 activity of Ubinas volcano (Peru):

881   petrology of the 2006 eruptive products and insights into genesis of andesite magmas, magma recharge and

882   plumbing system. J. Volcanol. Geotherm. Res. 270, 122–141.

883   Rivera. M., Martin, H., Le Pennec, J.L., Thouret, J.C., Gourgaud, A., Gerbe, M.C., 2017. Petro-geochemical

884   constraints on the source and evolution of magmas at El Misti volcano (Peru). Lithos 268-271, 240-259.

885   Robin, C., Camus, G., Gourgaud, A., 1991. Eruptive and magmatic cycles at Fuego de Colima volcano (Mexico).

886   J. Volcanol. Geotherm. Res. 45, 209–225.

887   Rutherford, M.J., Hill, P.M., 1993. Magma ascent rates from amphibole breakdown: an experimental study applied

888   to the 1980–1986 Mount St. Helens eruptions. J. Geophys. Res. 98, 19667–19685.

889   Rutherford, M.J., Devine, J.D., 2003. Magmatic conditions and magma ascent as indicated by hornblende phase

890   equilibria and reactions in the 1995–2002 Soufrière Hills magma. J. Petrol. 44, 1433–1454.

891   Ryan, J., Beck, S., Zandt, G., Wagner, L., Minaya, E., Tavera, H., 2016. Central Andean crustal structure from

892   receiver function analysis. Tectonophysics 682, 120-133.

893   Sainlot, N. Vlastélic, I., Nauret, F., Moune, S., Aguilera, F. 2020. Sr-Pb isotopes signatures at Lascar volcano

894   (Chile): Insight into crustal contamination of arc magmas ascending through a thick continental crust. J. S.

895   Am. Earth Sci. 101, 102599.

896   Samaniego, P., Le Pennec, J.L., Robin, C., Hidalgo, S., 2011. Petrological analysis of the pre-eruptive magmatic

897   process prior to the 2006 explosive eruptions at Tungurahua volcano (Ecuador). J. Volcanol. Geotherm. Res.

898   199, 69-84.

899   Scaillet, B., Evans, B.W., 1999. The 15 June 1991 Eruption of Mount Pinatubo: I. Phase equilibria and pre-eruption

900   P–T–fO2–fH2O conditions of the dacite magma. J. Petrol. 40, 381–411.

901   Schiano, P., Monzier, M., Eissen, J.P., Martin, H., Koga, K.T., 2010. Simple mixing as the major control of the

902   evolution of volcanic suites in the Ecuadorian Andes. Contrib. Mineral. Petrol. 160, 297–312.

903   Schiavi, F., Bolfan-Casanova, N., Withers, A.C., Médard, E., Laumonier, M., Laporte, D., Flaherty, T., Gomez-

904   Ulla, A., 2018. Water quantification in silicate glasses by Raman spectroscopy: correcting for the effects of

905   confocality, density and ferric iron. Chemical Geology 483, 312-331.

906   Schmidt, M.W., 1992. Amphibole composition in tonalite as a function of pressure: an experimental calibration

907   of the Al-in-hornblende barometer. Contrib, Mineral. Petrol. 110, 304-310.

908   Schmidt, M.W., Jagoutz, O., 2017. The global systematics of primitive arc melts. Geochem. Geophys. Geosyst.

909   18, 2817–2854.

910   Sisson, T.W., Ratajeski, K., Hankins, W.B., Glazner, A.F., 2005. Voluminous granitic magmas from common

911   basaltic sources. Contrib. Mineral. Petrol. 148, 635-661.

912   Siebert, L., Simkin. T., Kimberly, P., 2010. Volcanoes of the World. third ed. Smithsonian Institution and

913   University of California press, 551 pp

914   Smith, J.A., Mark, B.G., Rodbell, D.T., 2008. The timing and magnitude of mountain glaciation in the tropical

915   Andes. Journal of Quaternary Science 23, 609-634.

916   Sørensen, E.V., Holm. P.M., 2008. Petrological inferences on the evolution of magmas erupted in the Andagua

917   Valley, Peru (Central Volcanic Zone). J .Volcanol. Geotherm. Res. 177, 378-396.

918   Streck, M.J., 2008. Mineral textures and zoning as evidence for open system processes. Reviews in Mineralogy

919   and Geochemistry 69, 595–622.

920   Sun, S.S., McDonough, W.F., 1989. Chemical and isotopic systematics of oceanic basalts: implications for mantle

921   composition and processes. In: Saunders, A.D., Norry, M.J. (eds) Magmatism in the ocean basins. Special

922   Publication 42, Geological Society, London, pp 313–345

923   Thouret, J.C., Rivera, M., Wörner, G., Gerbe, M.C., Finizola, A., Fornari, M., Gonzales, K., 2005. Ubinas: the

924   evolution of the historically most active volcano in southern Peru. Bull. Volcanol. 67, 557–589.

925   Turner. S.J., Langmuir, C.H., Katz, R.F., Dungan, M.A., Escrig, S., 2016. Parental arc magma compositions

926   dominantly controlled by mantle-wedge thermal structure. Nat Geosci 9, 772.

927   Ulmer, P., Kaegi, R., Müntener, O., 2018. Experimentally derived intermediate to silica-rich arc magmas by

928   fractional and equilibrium crystallization at 1 0 GPa: an evaluation of phase relationships, compositions, liquid

929   lines of descent and oxygen fugacity. J. Petrol. 59, 11-58

930   White, W.M., McBirney, A.R., Duncan, R.A., 1993. Petrology and geochemistry of the Galapagos islands: portrait

931   of a pathological mantle plume. J. Geophys. Res. 98, 19533–19563.

932   Wright, H., Rivera, M., Vela, J., Harpel, C., 2017. Explosive eruptive history of Ubinas volcano, Peru, over the

933   past 14 ka. IAVCEI General Assembly, Portland, Oregon, August 14-18th, p. 1241.

934
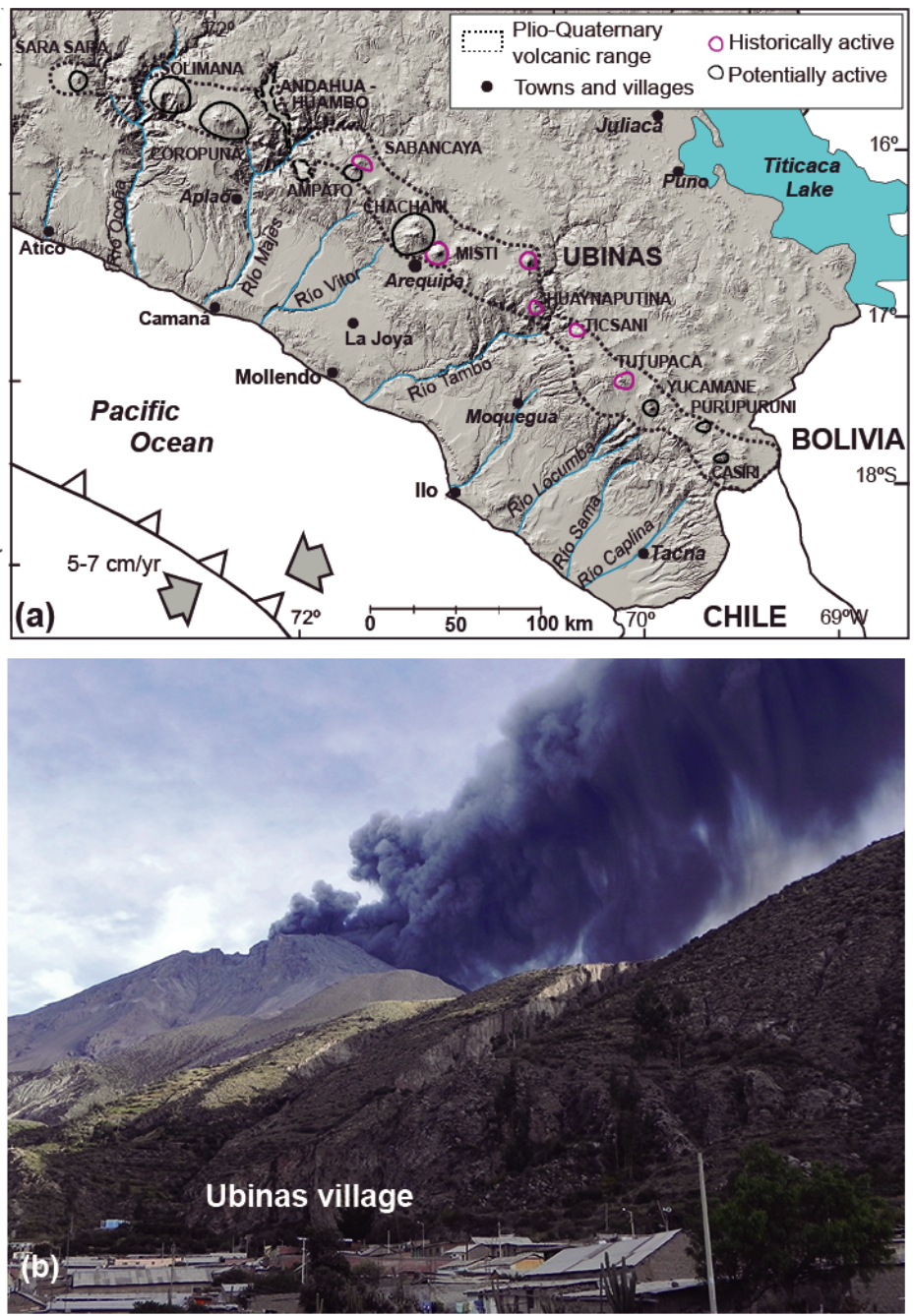
Figures

Figure 1. (a) Digital elevation model of southern Peru, showing the location of the active volcanic arc and Ubinas

volcano. **(b)** Ubinas volcano seen from the south, showing an ash-rich vulcanian eruption column. This photo was

taken from Ubinas village on April 26th, 2014.
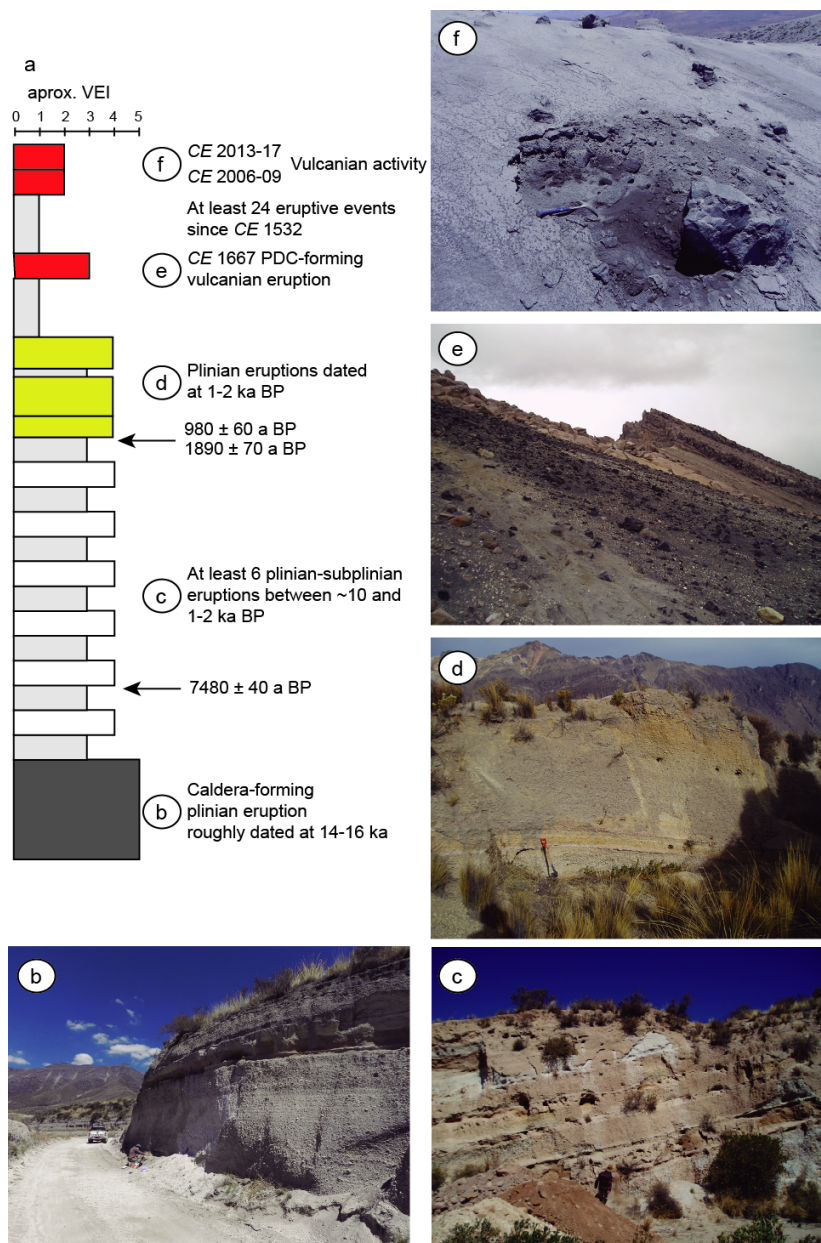
Figure 2. (a) Synthetic stratigraphic column showing the main eruptive events of the post-glacial to recent eruptive chronology of Ubinas volcano (after Thouret et al., 2005 and our own fieldwork). The colour code corresponds to the main units defined in the text: grey/black for rhyolites, white for dacites, yellow for andesites and red for basaltic andesites. **(b)** Plinian fallout deposit close to Sacuhaya hamlet (UBI-10-10, see Supplementary material 1 for the UTM location). **(c)** Succession of at least 6 plinian-subplinian fallout deposits interlayered with reworked ash horizons outcropping close to Sacuhaya hamlet (UBI-10-11 to UBI-10-16). **(d)** Plinian fallout deposits at Quebrada Infiernillos (UBI-10-01 to UBI-10-06) dated at 1-2 ka. **(e)** Scoria-rich pyroclastic density current deposit on the western flank of Ubinas just below the caldera rim (UBI-10-19). **(f)** Ballistic block near the caldera rim associated with the 2015 eruption (UBI-15-14). Note the grey ash layer that covers the caldera rim results from the recent eruptions (2006-2009 and 2013-2015).

955
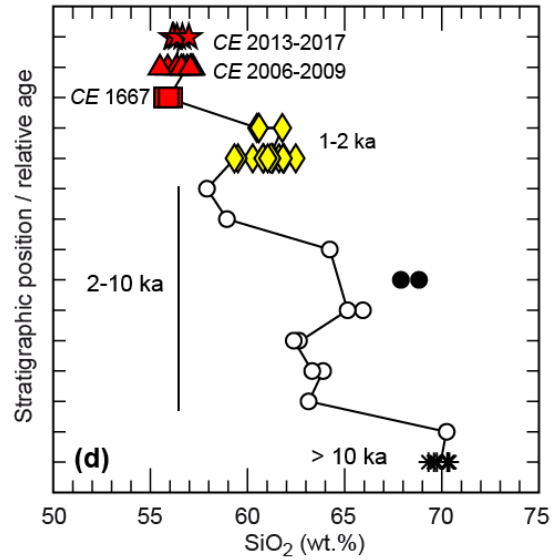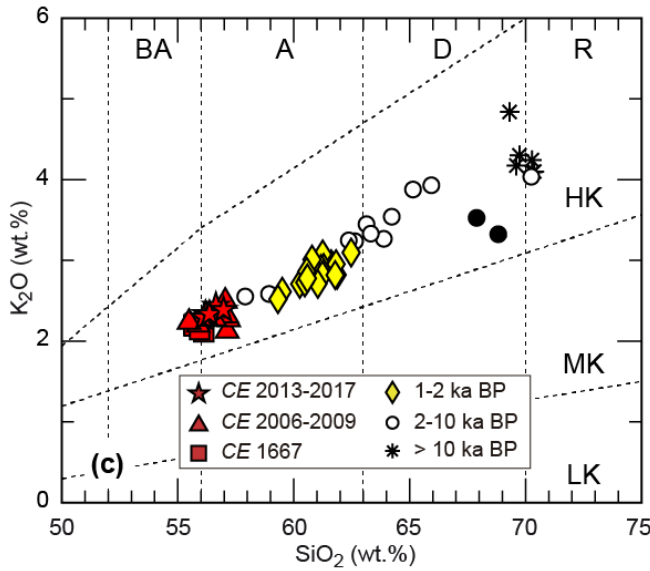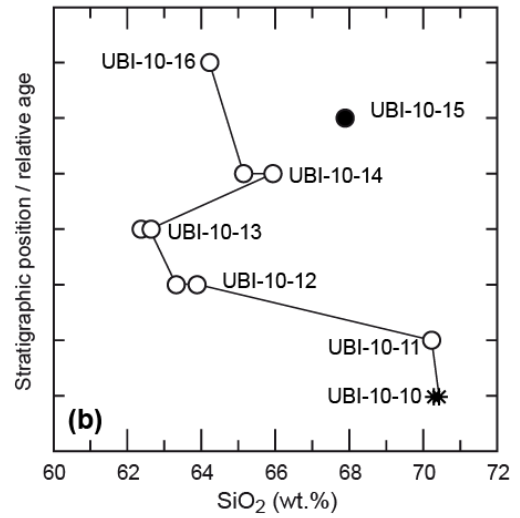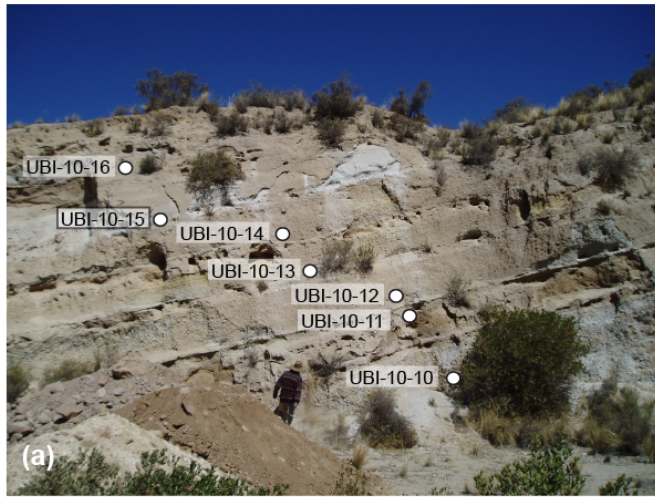
Figure 3. (a) Sample locations on the Sacuhaya cross-section. **(b)** Silica content of samples from the Sacuhaya

section. **(c)** K_2O *vs.* SiO_2 diagram from the post-glacial, historical, and recent samples of Ubinas volcano. The

fields in this diagram are taken from Peccerillo and Taylor (1976). BA, basic andesite; A, andesite; D, dacite; R,

rhyolite; LK, low potassium; MK, medium potassium; HK, high potassium. **(d)** Silica contents *vs.* stratigraphic

position for the post-glacial to recent samples. Black dots correspond to samples from a distal tephra fallout (UBI-

10-15 and UBI-10-08), whose source is probably other than Ubinas.

967
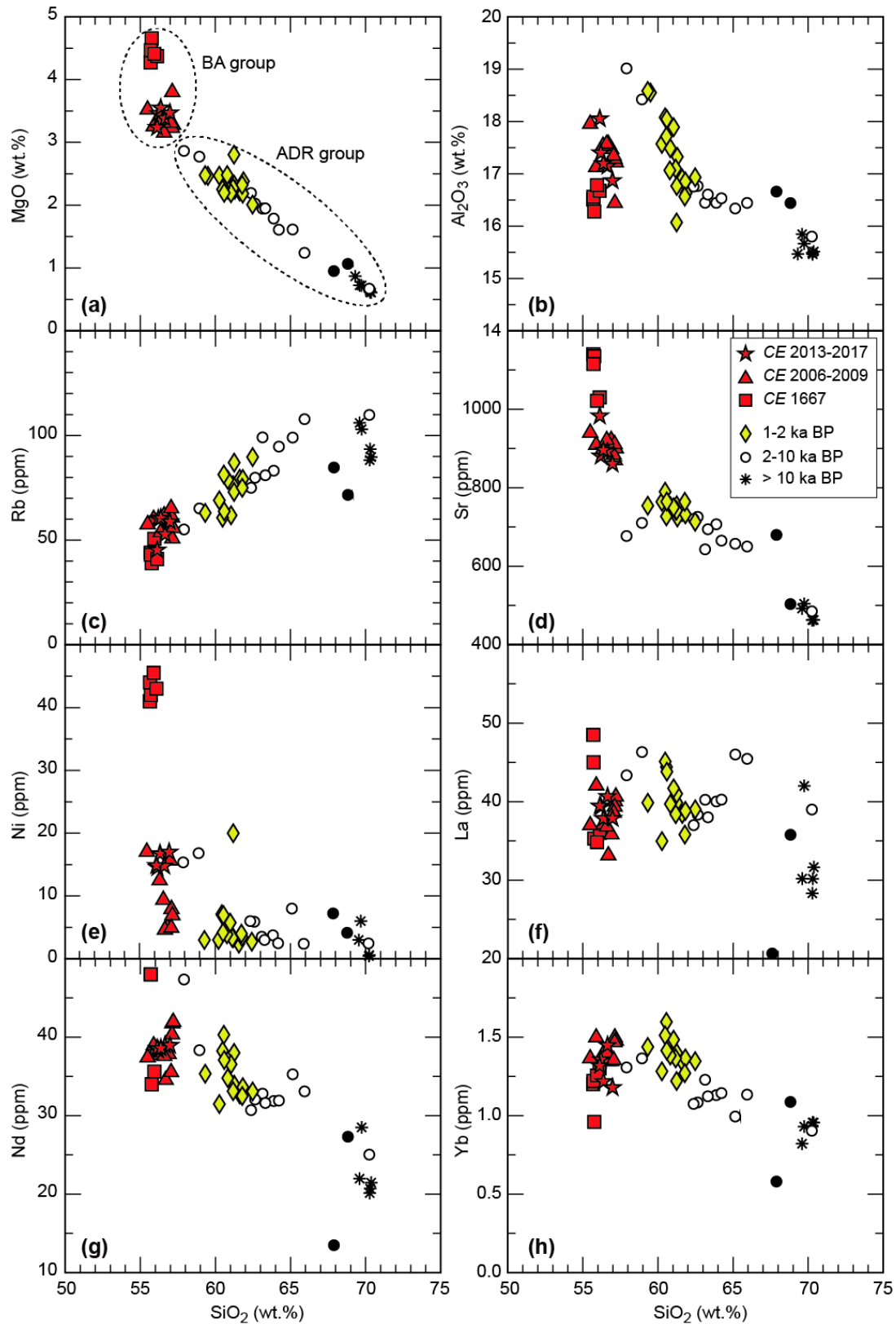
Figure 4. Selected major (**a**, **b**) and trace (**e, f, g, h**) elements for Ubinas samples. Note the break in slope between

the basic andesite (BA) group and the andesite, dacite, rhyolite (ADR) group. Symbols are the same as in Fig. 3.

971

972
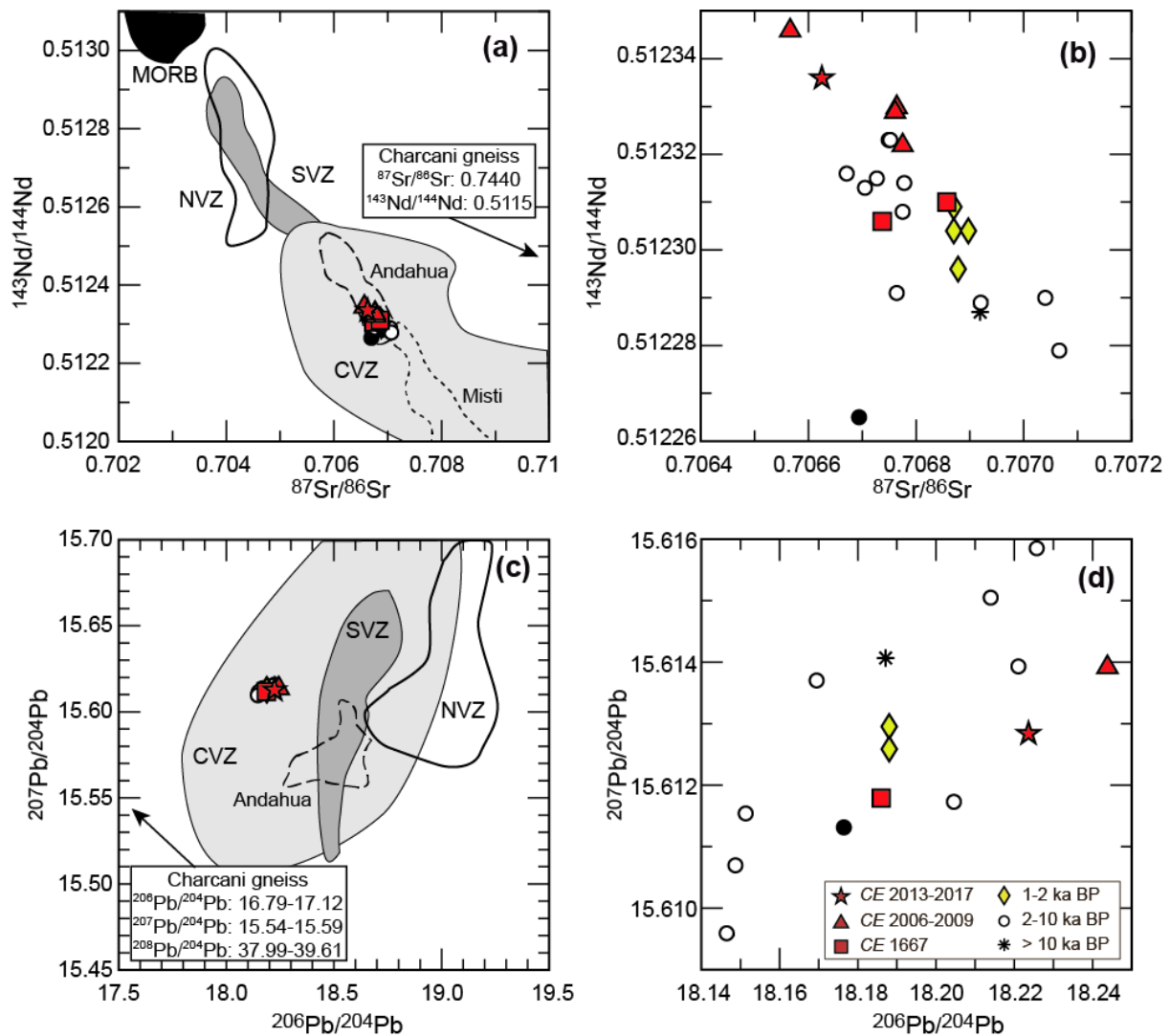
Figure 5. (a) $^{87}Sr/^{86}Sr$ *vs.* $^{143}Nd/^{144}Nd$ diagram for Ubinas rocks, compared with published isotopic data for the

Mid-Ocean Ridge Basalts (MORB, White et al., 1993 and reference therein) and the Andean Northern, Central

and Southern Volcanic Zones (NVZ, CVZ and SVZ respectively; Davidson et al., 1991; Ancellin et al., 2017). **(b)**

Detailed $^{87}Sr/^{86}Sr$ *vs.* $^{143}Nd/^{144}Nd$ diagram for Ubinas samples. **(c)** $^{206}Pb/^{204}Pb$ *vs.* $^{207}Pb/^{204}Pb$ diagram for Ubinas

samples. Note the extreme homogeneity of Ubinas volcano compared to the very large field displayed for the CVZ.

(d) Detailed $^{206}Pb/^{204}Pb$ *vs.* $^{207}Pb/^{204}Pb$ diagram for Ubinas samples. The absence of linear correlation suggests that

a process more complicated than a simple binary mixing process controls Pb isotopes variations. Data from the

Andahua monogenetic cones (Delacour et al., 2007) and El Misti volcano (Rivera et al., 2017) are also included.

The isotopic signature of the Precambrian Charcani gneiss comes from Boily et al. (1990), Mamani et al. (2010)

and Rivera et al. (2017). Symbols are the same as in Fig. 3. Analytical error bars are within the symbol size.

983
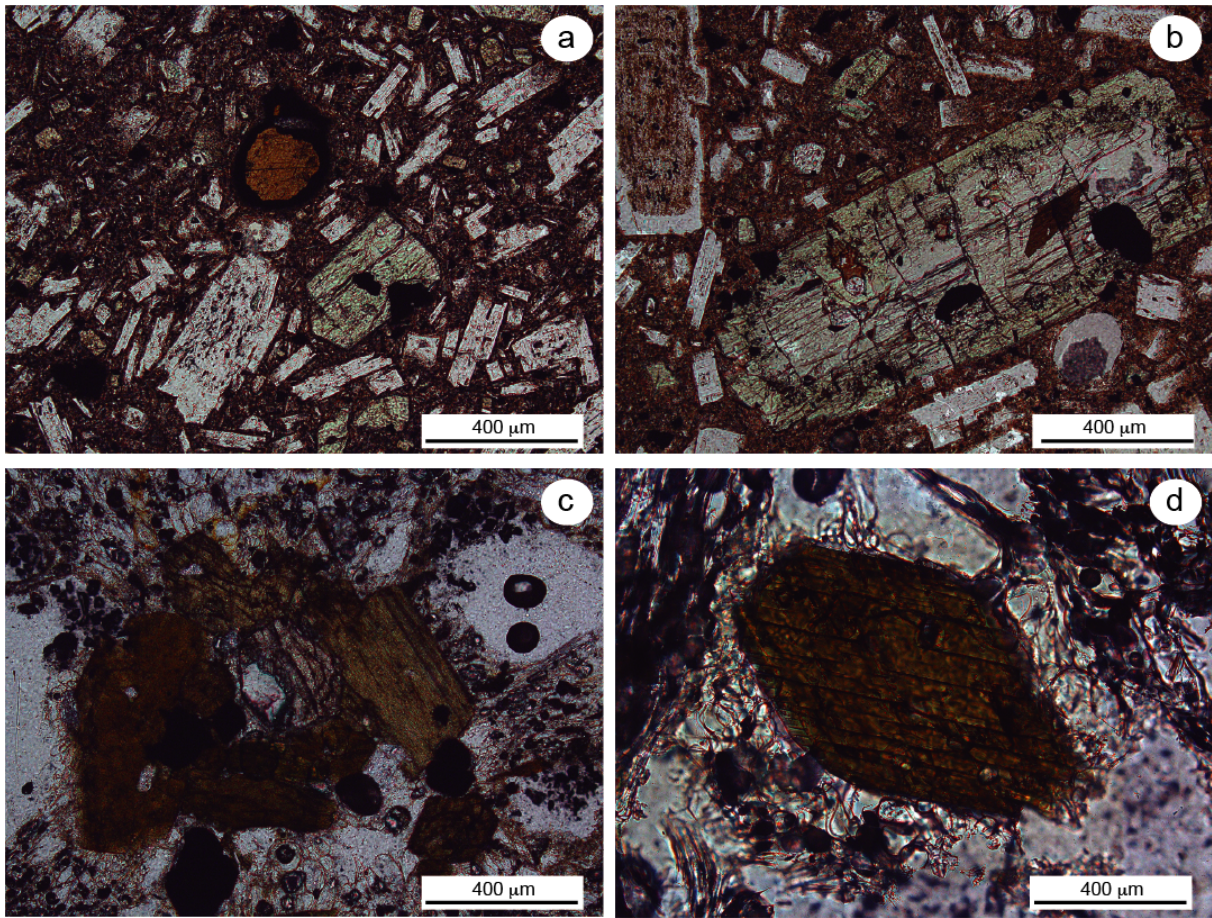
Figure 6. Optical microphotographs for Ubinas samples. (**a**) Basaltic andesite (UBI-10-18C) showing a mineral assemblage composed of plagioclase, ortho- and clinopyroxene, amphibole and Fe-Ti oxides. Note the black aureole around the amphibole. (**b**) Disequilibrium textures in the basaltic andesite (UBI-10-18C) showing a clinopyroxene phenocryst core mantled with an overgrowth rim and a plagioclase phenocryst (top left) with an altered (sieve) core and a fresh overgrowth rim. (**c**) Andesitic tephra (UBI-10-06) showing a mineral clot composed of plagioclase, amphibole and orthopyroxene. (**d**) Amphibole phenocryst in a rhyolitic tephra (UBI-10-10B).

993
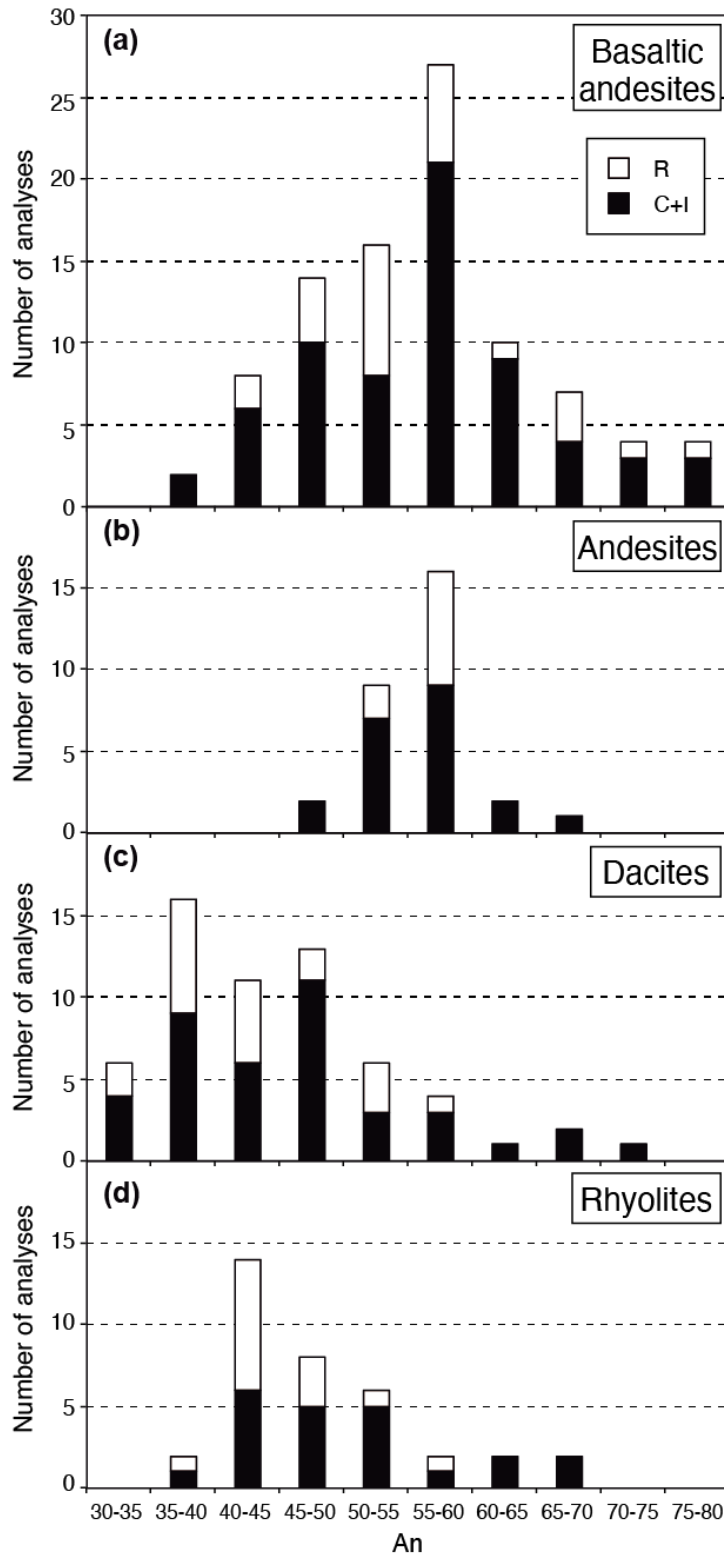
Figure 7. Histograms of An contents for plagioclases derived from (**a**) basaltic andesites, (**b**) andesites, (**c**) dacites, and (**d**) rhyolites. Rims (R) are differentiated from core and interior (C+I) compositions. Note the large An variations, namely for plagioclase from the BA group, and the fact that most compositions in the BA (and andesites) display An_{55-65}, whereas the plagioclases in the dacites and rhyolites are generally between An_{35-50}.

998

999
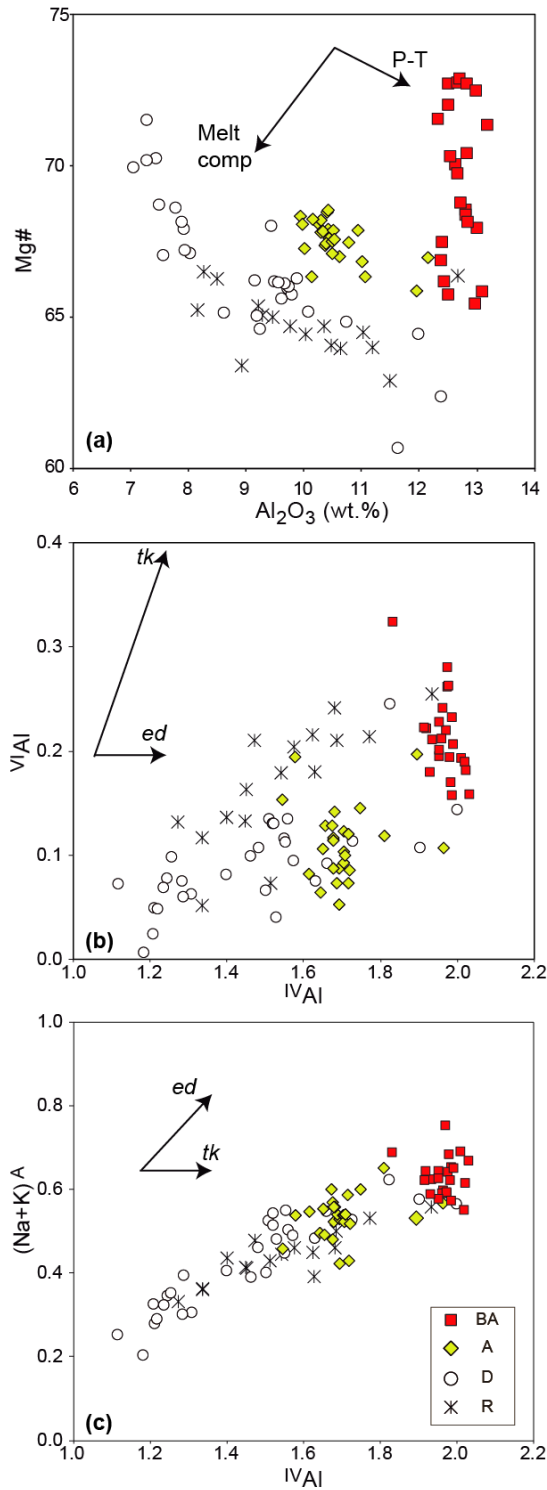
Figure 8. (a) Diagram showing the Al_2O_3 and Mg# variations for Ubinas amphiboles. The vectors represent in a schematic way the effect of an increase in P-T as well as a variation of mafic to felsic magma chemistry (modified from Kiss et al., 2014). **(b)** ^{IV}Al *vs.* ^{VI}Al, and **(c)** ^{IV}Al *vs.* $(Na+K)^A$ showing the effect of edenite (*ed*) and tshermakite (*tk*) substitutions (after Poli and Schmidt, 1992).

1004

1005
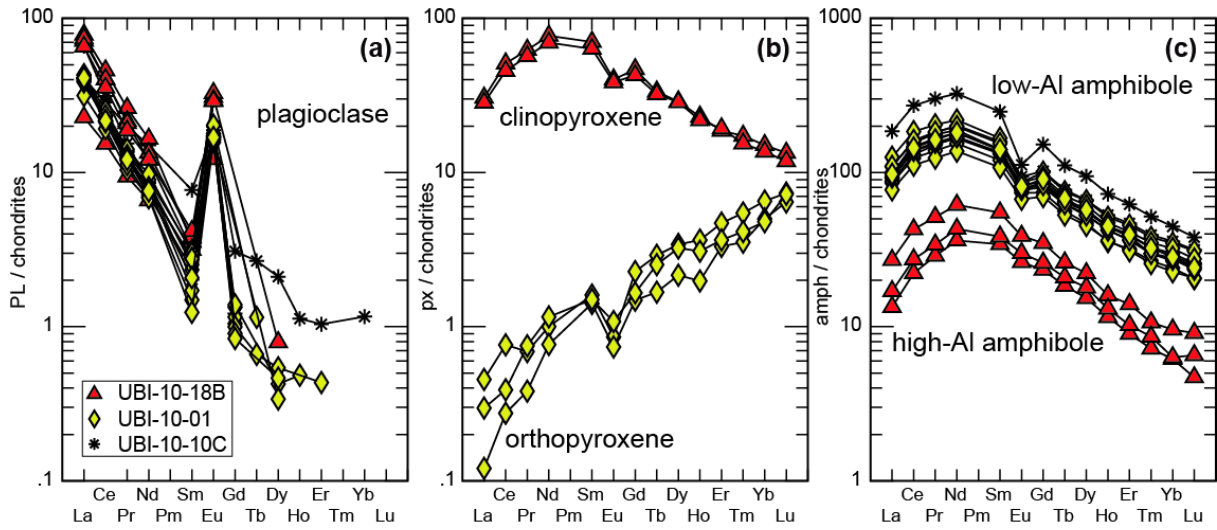
Figure 9. Rare earth element (REE) diagram for selected (**a**) plagioclase, (**b**) ortho and clinopyroxene, and (**c**) amphibole phenocrysts from Ubinas samples. Note that two populations exist for amphibole. Data normalized to chondrite values (Sun and McDonough, 1989). Data correspond to a basaltic andesite (UBI-10-18B), an andesite (UBI-10-01) and a rhyolite (UBI-10-10C).

1012
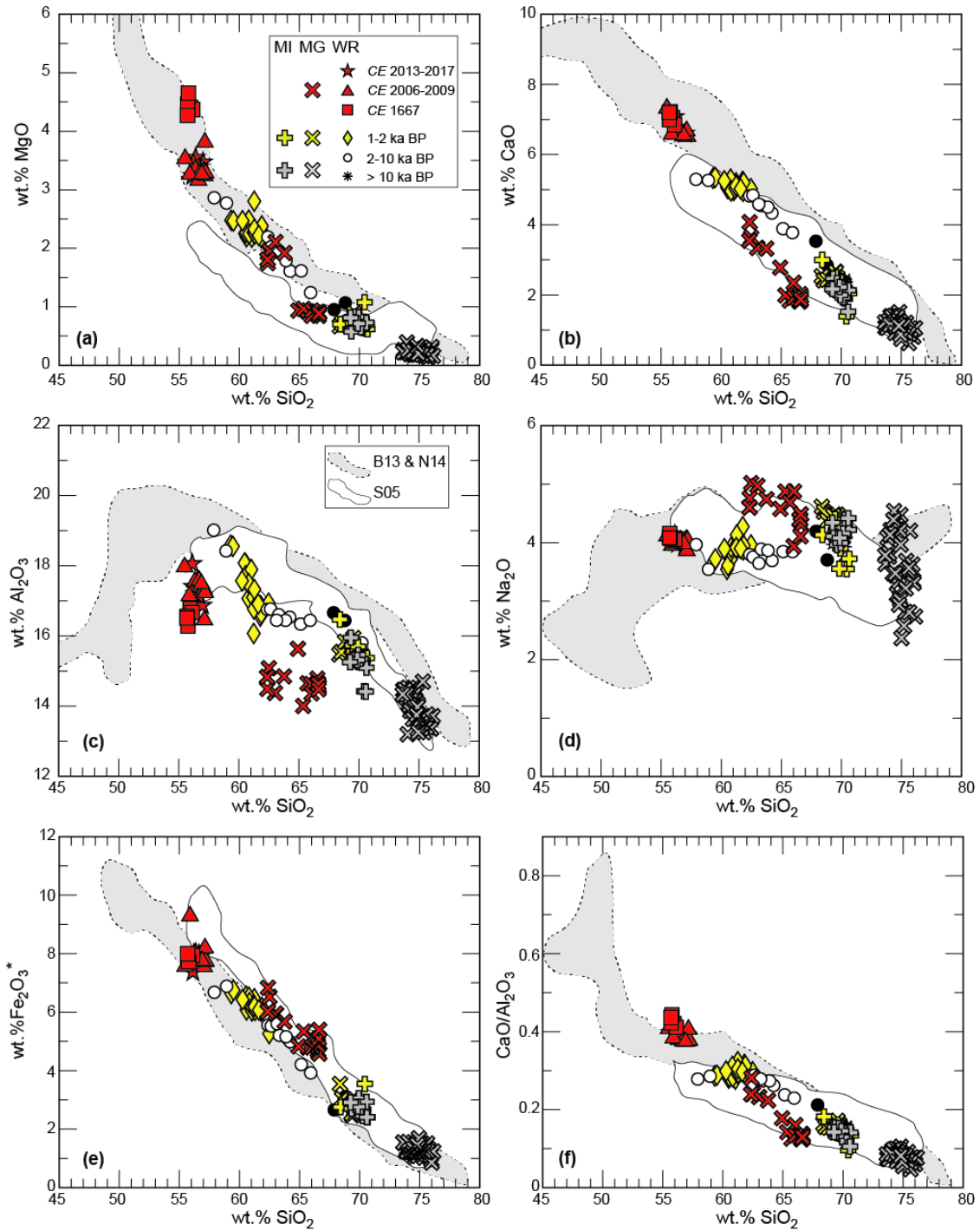
Figure 10. MgO **(a)**, CaO **(b)**, Al_2O_3 **(c)**, Na_2O **(d)**, $Fe_2O_3^*$ **(e)**, CaO/Al_2O_3 **(f)** as a function of silica for whole-rocks (WR), matrix glasses (MG) and melt inclusions (MI) of Ubinas samples. The fields of experimentally determined liquid-line-of-descent compositions are shown for comparison (S05: Sisson et al., 2005; B13: Blatter et al., 2013; N14: Nandedkar et al., 2014).

1020
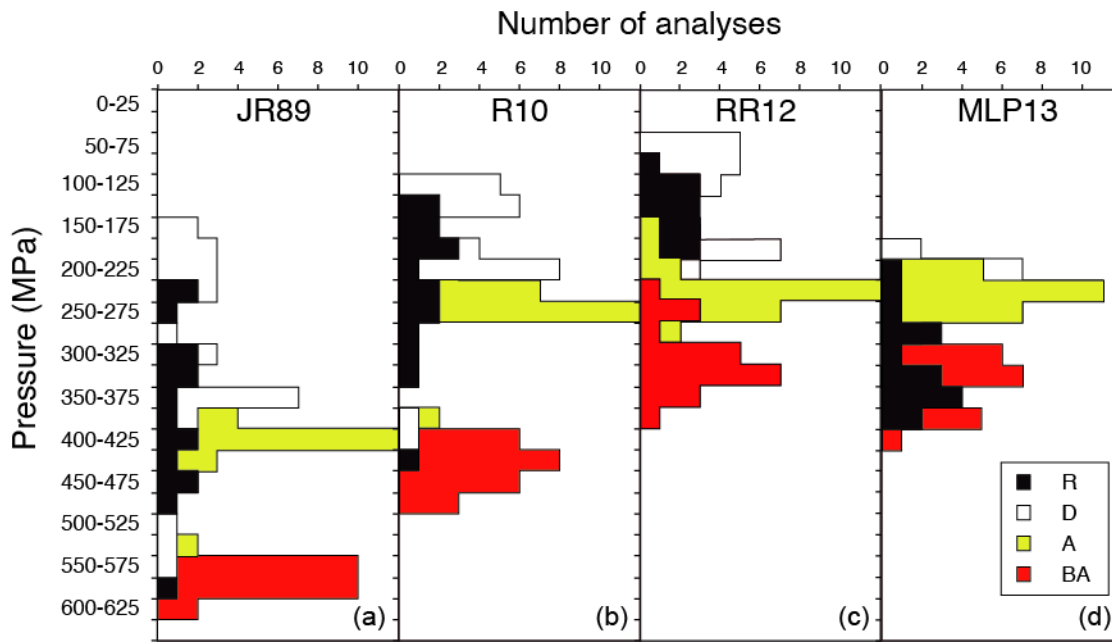
1021

1022

1023 **Figure 11.** Histograms of amphibole crystallization pressure estimates for Ubinas samples (BA: basic andesites;

1024 A: andesites; D: dacites; R: rhyolites). Different models have been tested (JR89: Johnson and Rutherford, 1989;

1025 R10: Ridolfi et al., 2010; RR12: Ridolfi and Renzulli, 2012; MLP: Médard and Le Pennec, 2013).
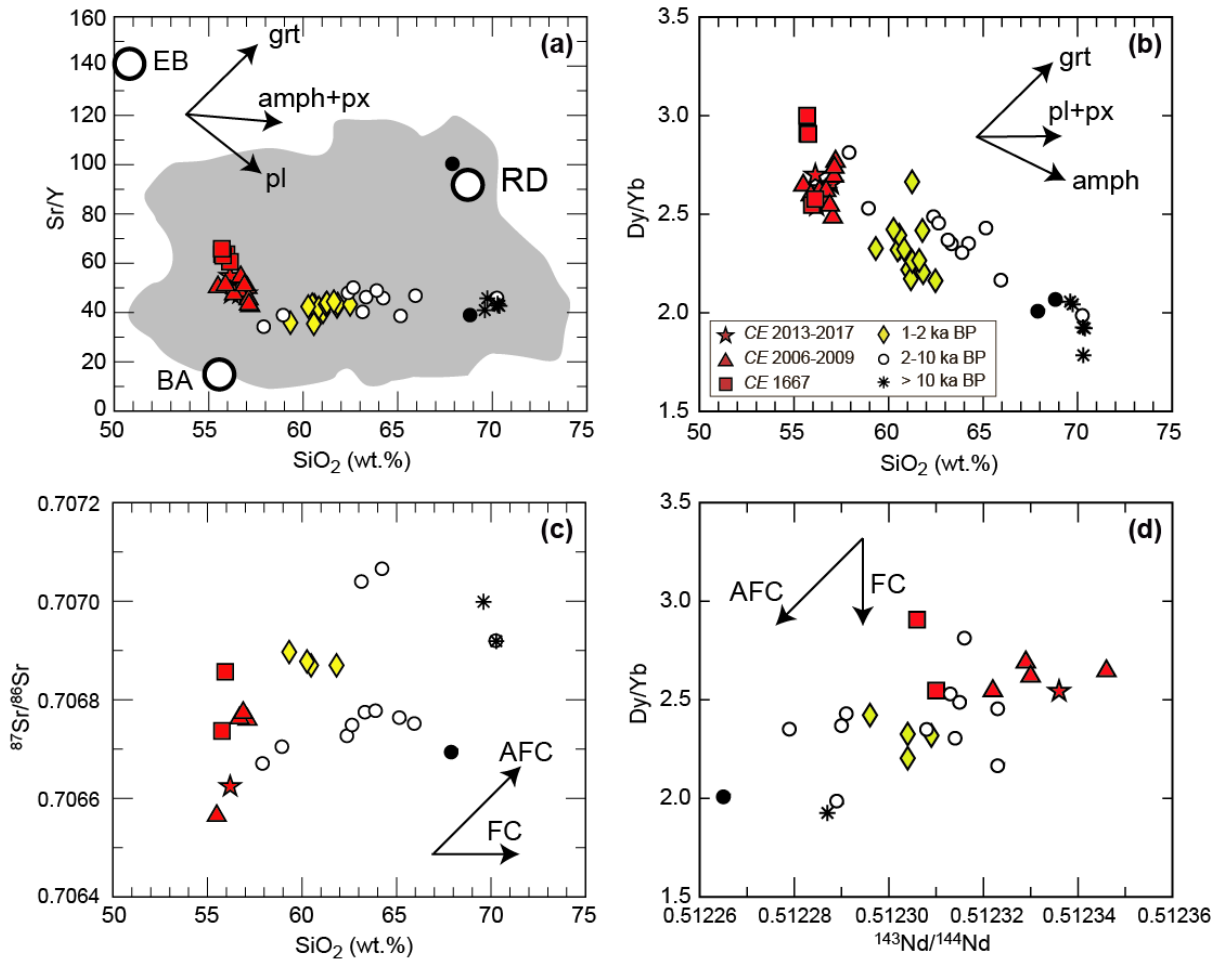
Figure 12. (a, b, c) Sr/Y, Dy/Yb, and ^{87}Sr/^{86}Sr *vs.* silica content. **(d)** Dy/Yb *vs.* ^{143}Nd/^{144}Nd. The white cercles labelled as "BA", "EB" and "RD" correspond to the three end-members identified by Blum-Oeste and Wörner (2016). BA – calc-alkaline basaltic andesite, EB – shoshonitic enriched basalt, RD – crustal-derived rhyodacite. The grey field corresponds to the CVZ geochemical variation. The arrows in (a, b) show the expected effects of garnet, amphibole and plagioclase-pyroxene fractionation. Note that the only mineral able to efficiently fractionate MREE over HREE (i.e. Dy/Yb) is amphibole. The arrows in (c, d) correspond to theoretical trends for FC and AFC process. Symbols are the same as in Fig. 3.
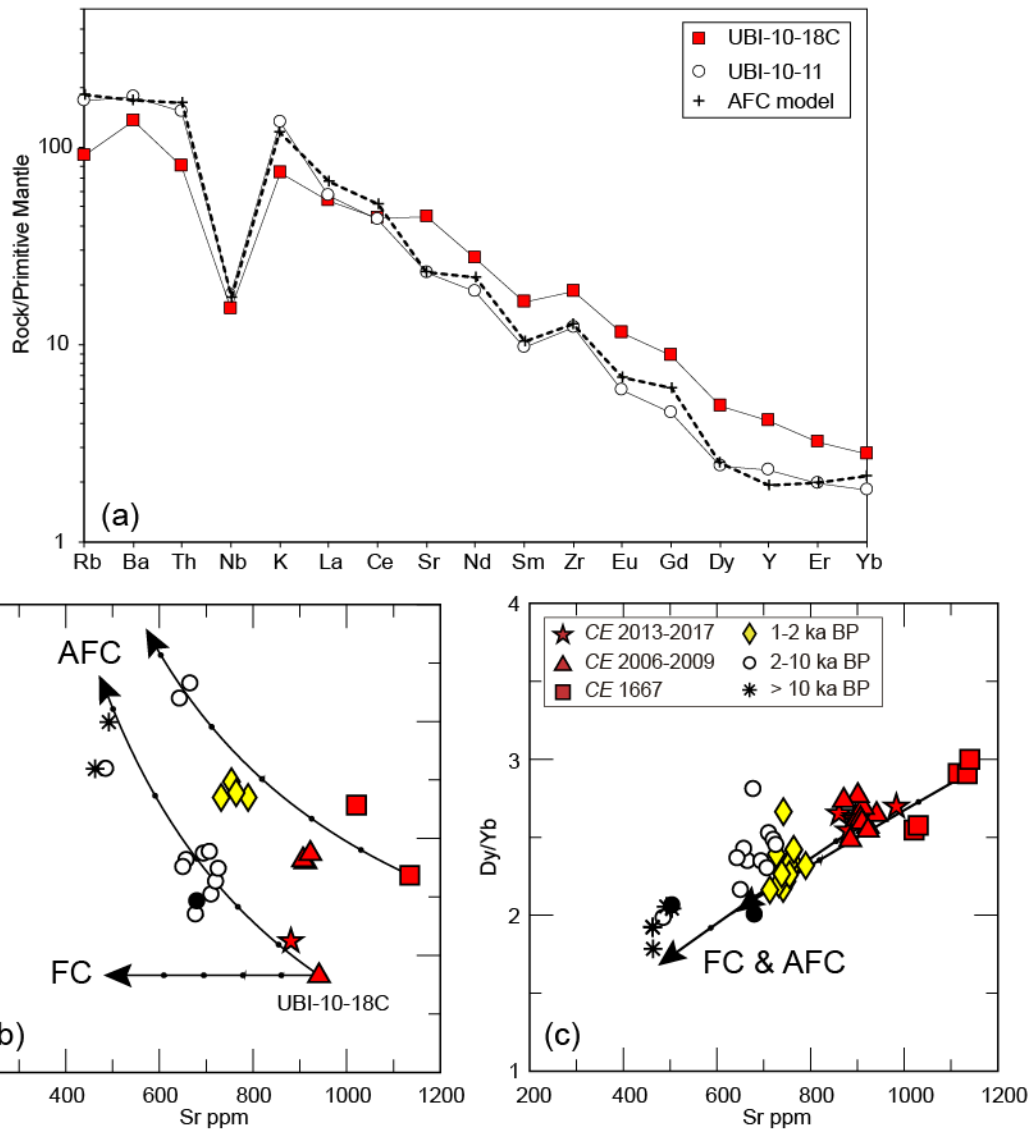
Figure 13. Results of the geochemical modelling. (**a**) Multielement diagram normalized to Primitive Mantle (Sun and McDonough, 1989) for the mafic (UBI-10-18C) and silica-rich (UBI-10-11) end-members, as well as an AFC model. (**b**) Sr *vs.* $^{87}Sr/^{86}Sr$ diagrams showing the Ubinas samples as well as the AFC and FC models from two mafic end-members (UBI-10-18C and UBI-99-10). (**c**) Sr *vs.* Dy/Yb diagram for Ubinas sampled and the two AFC models. The fractionating phases for both models (FC and AFC) are 46% Pl + 44% Amph + 3%Cpx + 6% Mag + 1%Apt, and the assimilation/fractional crystallization rate (r) = 0.04. Partition coefficients were compiled by Rivera et al. (2017) and correspond to intermediate to acid liquids. Note that in (a) and (c) AFC and FC models display almost the same values due to fact that trace elements are slightly modified by the very low degrees of crustal assimilation, whereas in (b) we clearly show that assimilation is needed for explain the Sr isotopic variation. Symbols are the same as in in Fig. 3.

45
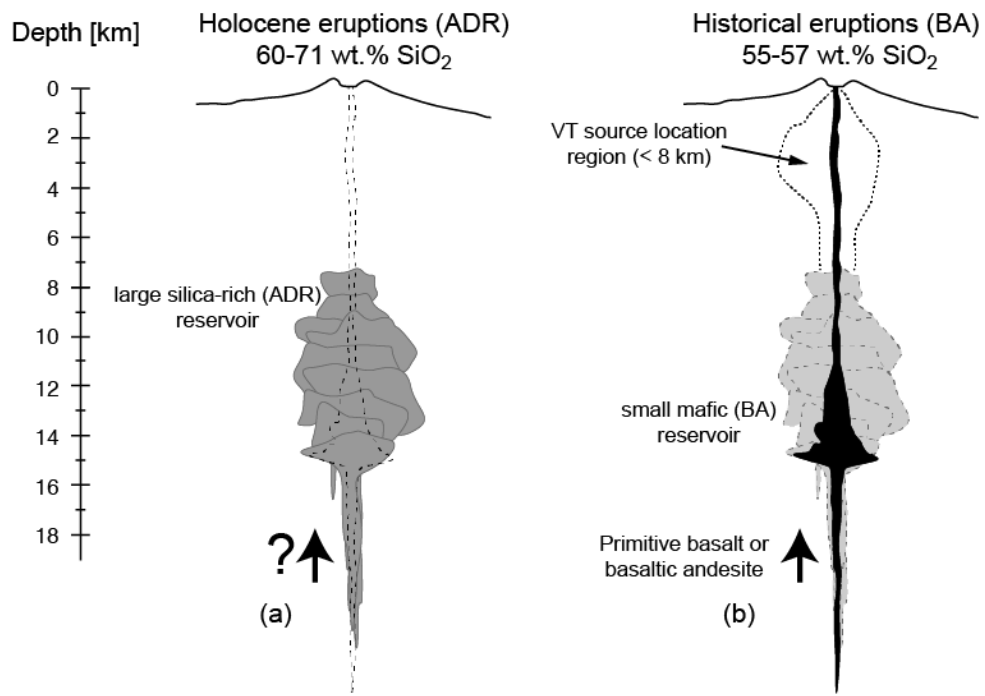
Figure 14. Reconstruction of the magmatic plumbing system beneath Ubinas volcano for **(a)** the ADR group (post glacial and Holocene), and **(b)** the BA group (Historical and recent eruptions). The volcano-tectonic (VT) seismic source location comes from Machacca-Puma et al. (2019).

Table 1. Whole-rock major, trace elements and Sr-Nd-Pb isotopes for the Ubinas

Sample No.	UBI-10-10A	UBI-10-10B	UBI-10-10C	UBI-10-11	UBI-10-07	UBI-10-12	UBI-10-13	UBI-10-14	UBI-10-15	UBI-10-08	UBI-10-16	UBI-10-09	UBI-13-05	UBI-10-01A	UBI-10-01B	UBI-10-02
Estimated Age / Volcanic unit	>10 ka	>10 ka	>10 ka	2-10 ka	2-10 ka	2-10 ka	2-10 ka	2-10 ka	2-10 ka	2-10 ka	2-10 ka	2-10 ka	2-10 ka	1-2 ka	1-2 ka	1-2 ka
Stratigraphic position	1	1	1	2	3	4	5	6	7	7	8	9	10	11	11	11
SiO_2 (wt.%)	66,80	66,32	66,99	66,78	61,30	61,85	60,19	62,78	65,30	64,88	61,75	55,61	53,24	59,30	59,61	59,59
TiO_2	0,33	0,33	0,33	0,35	0,75	0,67	0,74	0,53	0,35	0,36	0,64	1,03	1,06	0,84	0,88	0,76
Al_2O_3	14,69	14,62	14,77	15,02	15,97	15,92	16,11	15,66	16,03	16,03	15,89	17,38	17,48	16,28	16,32	16,15
$Fe_2O_3^*$	2,34	2,31	2,28	2,54	5,44	4,99	5,31	3,73	2,56	2,94	2,94	6,50	6,14	5,84	6,03	5,02
MnO	0,07	0,07	0,07	0,07	0,09	0,10	0,10	0,08	0,05	0,09	0,09	0,11	0,08	0,10	0,10	0,09
MgO	0,58	0,61	0,58	0,64	1,89	1,73	1,95	1,18	0,91	1,00	1,55	2,62	2,63	2,14	2,26	1,92
CaO	2,33	2,29	2,26	2,26	4,45	4,36	4,65	3,59	3,40	2,68	4,17	4,97	4,87	4,84	4,97	4,79
Na2O	3,86	3,71	3,89	3,46	3,54	3,74	3,74	3,61	3,66	4,03	3,49	3,55	3,34	3,65	3,75	3,78
K2O	3,89	4,00	3,90	3,84	3,35	3,16	3,11	3,74	3,39	3,13	3,40	2,44	2,35	2,84	2,99	2,95
P_2O_5	0,12	0,12	0,11	0,12	0,32	0,29	0,33	0,26	0,16	0,20	0,37	0,44	0,32	0,35	0,33	0,33
LOI**	3,87	3,87	3,75	4,57	2,57	2,54	3,13	3,80	2,97	4,84	2,85	5,39	8,45	3,23	1,94	4,35
Total	98,89	98,24	98,94	99,63	99,66	99,36	99,21	99,02	99,16	99,11	98,99	99,76	100,39	99,48	99,27	99,73
Sc (ppm)	2,88	2,74	2,69	3,17	7,53	6,73	7,37	4,79	4,28	5,63	6,63	10,55	8,93	7,98	8,33	7,38
V	26,42	25,62	25,33	30,37	95,58	81,20	92,35	60,01	50,32	38,74	79,79	125,32	120,61	103,26	108,08	84,78
Cr	1,09	1,20	1,02	3,06	4,36	5,95	9,24	5,65	5,63	7,26	3,28	23,47	18,55	3,54	4,92	4,09
Co	3,64	3,25	3,36	2,18	12,83	10,16	11,50	6,92	6,61	6,10	9,98	17,74	18,45	12,26	13,34	10,60
Ni	0,60	0,45	0,00	2,45	3,51	3,74	5,90	2,39	7,23	4,15	2,48	16,82	15,36	2,42	3,32	2,72
Rb	93,50	88,24	89,71	109,81	99,09	83,17	79,81	107,79	84,68	71,61	94,67	65,13	55,10	79,32	87,03	89,67
Sr	463,36	462,58	462,90	484,95	642,78	706,67	725,53	650,03	679,59	503,43	664,96	710,14	676,78	738,37	755,05	713,07
Y	10,78	10,61	10,83	10,56	15,96	14,44	14,47	13,87	6,77	12,91	14,50	18,22	19,74	16,60	17,17	16,47
Zr	130,28	131,26	130,73	136,74	127,04	99,13	111,85	162,32	43,91	80,58	107,47	223,48	256,67	232,57	232,41	235,46
Nb	11,57	11,81	11,22	12,95	8,28	10,74	11,74	4,82	10,70	11,22	10,95	12,19	13,15	11,03	11,60	10,88
Ba	1186,54	1172,69	1181,56	1263,81	1087,45	1143,87	1150,38	1235,08	971,02	1144,00	1107,36	933,40	968,40	1113,09	1111,79	1113,35
La	30,17	28,32	31,64	38,99	40,23	40,02	38,34	45,45	17,42	35,77	40,25	46,31	43,35	38,42	39,86	39,01
Ce	65,38	62,76	68,09	77,02	80,18	78,20	77,96	84,48	38,45	71,02	80,61	83,45	73,55	75,89	78,45	76,02
Nd	20,71	20,13	21,47	25,04	32,81	31,87	32,06	33,09	13,50	27,31	31,92	38,34	47,35	32,70	33,95	33,08
Sm	4,19	3,99	3,91	4,31	5,93	5,79	5,83	5,70	2,62	4,78	5,93	6,76	8,25	6,04	6,37	6,11
Eu	0,86	0,91	0,90	0,99	1,42	1,42	1,44	1,28	0,78	1,08	1,26	1,70	1,80	1,56	1,64	1,43
Gd	2,53	2,72	2,87	2,67	4,28	3,78	3,98	3,66	1,81	3,17	4,17	4,86	6,06	4,09	4,38	4,40
Dy	1,71	1,80	1,83	1,79	2,91	2,60	2,66	2,45	1,16	2,25	2,69	3,45	3,68	3,04	3,16	2,91
Er	0,80	0,84	0,69	0,95	1,64	1,35	1,32	1,21	0,53	1,08	1,29	1,51	1,30	1,42	1,57	1,52
Yb	0,96	0,93	0,96	0,90	1,23	1,13	1,08	1,13	0,58	1,09	1,14	1,36	1,31	1,34	1,40	1,35
Th	12,35	11,70	12,10	12,88	9,87	9,05	8,95	12,44	6,71	5,84	10,05	10,62	10,65	8,75	8,60	9,20
$^{87}Sr/^{86}Sr$		0,706919		0,706920	0,707040	0,706778	0,706749	0,706752	0,706694			0,707066	0,706705	0,706671		
±		0,000007		0,000006	0,000007	0,000009	0,000006	0,000005	0,000007			0,000005	0,000007	0,000005		
$^{143}Nd/^{144}Nd$		0,512287		0,512289	0,512290	0,512314	0,512323	0,512323	0,512265			0,512279	0,512313	0,512316		
±		0,000005		0,000009	0,000005	0,000004	0,000005	0,000007	0,000004			0,000004	0,000008	0,000005		
$^{206}Pb/^{204}Pb$		18,1871		18,1695	18,1487	18,2257	18,2210	18,2139	18,1764			18,1514	18,1465	18,2045		
±		0,0007		0,0007	0,0004	0,0009	0,0003	0,0007	0,0006			0,0003	0,0006	0,0004		
$^{207}Pb/^{204}Pb$		15,6141		15,6107	15,6107	15,6159	15,6139	15,6150	15,6113			15,6115	15,6096	15,6117		
±		0,0007		0,0007	0,0004	0,0008	0,0003	0,0006	0,0006			0,0003	0,0006	0,0003		
$^{208}Pb/^{204}Pb$		38,5961		38,6136	38,5601	38,5764	38,5720	38,5660	38,6486			38,5681	38,5708	38,5731		
±		0,0019		0,0017	0,0010	0,0022	0,0009	0,0017	0,0017			0,0008	0,0017	0,0008		

Table 1. Continued

Sample No.	UBI-10-03	UBI-10-04	UBI-10-05	UBI-14-01A	UBI-10-06	UBI-14-01C	UBI-14-01B	UBI-10-19	UBI-10-20	UBI-10-18A	UBI-10-18B	UBI-10-18C	UBI-14-12	UBI-14-04	UBI-14-03	UBI-15-14	UBI-15-02
Estimated Age / Volcanic unit	1-2 ka	1-2 ka	1-2 ka	1-2 ka	1-2 ka	1-2 ka	1-2 ka	1667 CE	2006-2009 CE	2006-2009 CE	2006-2009 CE	2006-2009 CE	2014-2015 CE	2014-2015 CE	2014-2015 CE	2014-2015 CE	2014-2015 CE
Stratigraphic position	11	11	11	11	12	12	12	13	14	14	14	14	15	15	15	15	15
SiO_2 (wt.%)	59,60	58,96	58,64	58,31	57,73	57,66	56,91	55,55	56,19	56,77	56,54	55,40	56,12	55,85	54,70	55,57	55,88
TiO_2	0,84	0,86	0,87	0,84	0,88	0,87	0,83	1,28	1,18	1,16	1,13	1,23	1,23	1,17	1,12	1,19	1,17
Al_2O_3	16,25	16,48	16,86	17,09	16,89	17,24	16,95	16,66	17,50	17,27	17,56	17,93	17,38	16,91	17,60	16,96	16,55
$Fe_2O_3^*$	5,83	6,01	6,10	5,77	6,24	6,15	5,71	7,74	7,98	7,51	7,92	7,55	7,98	7,87	7,18	7,91	7,81
MnO	0,10	0,10	0,10	0,10	0,10	0,10	0,10	0,11	0,12	0,11	0,12	0,11	0,12	0,11	0,11	0,11	0,11
MgO	2,11	2,19	2,17	2,09	2,17	2,15	2,06	4,38	3,34	3,30	3,16	3,52	3,46	3,34	3,16	3,50	3,41
CaO	4,78	4,85	4,79	4,76	4,79	4,84	4,87	7,00	6,65	6,50	6,68	7,30	6,76	6,52	6,89	6,65	6,47
Na2O	3,74	3,79	3,78	3,63	3,44	3,38	3,54	4,00	4,04	4,04	4,04	4,10	4,00	3,97	4,03	3,92	3,88
K2O	2,85	2,79	2,81	2,59	2,73	2,60	2,61	2,13	2,28	2,49	2,28	2,24	2,34	2,41	2,24	2,31	2,34
P_2O_5	0,32	0,34	0,30	0,35	0,36	0,36	0,34	0,45	0,47	0,41	0,48	0,44	0,48	0,45	0,43	0,45	0,45
LOI**	3,35	3,52	2,98	4,62	4,51	3,98	4,46	-0,09	-0,15	-0,03	-0,15	-0,25	-0,25	-0,12	-0,23	-0,31	-0,21
Total	99,75	99,89	99,40	100,14	99,84	99,32	98,39	99,59	99,99	99,66	99,76	99,58	99,62	98,48	97,23	98,27	97,87
Sc (ppm)	7,87	8,19	8,22	7,20	8,94	7,18	7,30	15,55	11,39	12,25	10,43	13,33	11,50	10,79	10,52	11,03	10,83
V	101,89	105,89	107,97	98,22	107,29	108,76	99,54	184,74	160,59	164,53	153,42	168,68	159,06	166,34	155,41	161,42	157,42
Cr	3,39	3,73	4,04	6,06	4,33	6,73	6,49	109,94	14,41	21,10	9,86	27,55	14,41	16,06	14,72	17,03	17,07
Co	12,76	13,03	13,23	12,81	15,23	17,76	13,58	24,45	20,69	19,49	19,25	19,84	20,86	21,49	18,77	20,16	20,65
Ni	3,47	3,33	3,30	5,76	4,20	7,08	6,97	45,53	12,58	15,75	9,47	17,12	14,57	14,82	14,91	16,79	17,02
Rb	79,22	76,24	78,81	61,86	81,34	60,71	63,75	50,64	53,89	65,48	62,02	57,75	60,29	52,89	45,41	60,67	58,89
Sr	732,01	741,53	753,04	749,82	726,84	789,63	764,59	1021,02	899,41	884,80	922,20	941,05	881,01	892,73	983,25	896,22	861,05
Y	16,83	17,11	17,95	18,64	20,50	18,28	17,80	16,03	18,86	17,61	18,81	18,60	18,39	18,64	17,92	18,31	18,02
Zr	230,72	232,73	237,78	266,90	245,37	264,10	255,43	190,48	210,35	204,70	213,76	207,40	210,29	215,40	211,70	217,23	214,48
Nb	8,28	11,22	11,81	12,35	11,17	12,55	11,62	11,35	11,44	11,18	11,18	10,78	11,02	11,01	10,61	11,45	11,73
Ba	1095,69	1111,34	1117,04	1265,60	1100,92	1181,80	1193,66	1043,91	1151,70	983,63	959,78	946,10	958,27	993,09	949,39	1144,71	1124,02
La	38,82	38,40	39,70	41,69	44,41	45,10	43,81	34,82	37,13	38,64	36,84	37,04	39,37	40,68	39,48	37,87	37,90
Ce	77,76	77,64	80,15	83,70	88,16	84,98	88,19	75,28	79,69	79,91	77,56	79,85	79,85	76,51	75,48	79,16	79,16
Nd	33,63	33,12	34,78	36,55	40,31	38,25	37,09	35,60	38,11	35,59	37,67	37,47	38,35	38,99	38,60	38,61	38,97
Sm	6,06	5,82	6,27	6,30	7,40	6,65	5,90	7,10	7,66	6,69	7,11	7,28	7,07	6,49	6,50	7,11	6,96
Eu	1,53	1,60	1,56	1,65	1,67	1,60	1,71	1,74	1,90	1,71	1,82	1,92	1,75	1,81	1,90	1,77	1,79
Gd	4,40	4,51	4,61	5,11	5,40	4,90	5,30	4,88	5,13	4,68	5,59	5,23	5,46	5,06	5,95	4,99	5,31
Dy	3,01	2,96	3,21	3,29	3,82	3,50	3,29	3,20	3,65	3,37	3,61	3,62	3,46	3,79	3,56	3,21	3,13
Er	1,42	1,19	1,62	2,24	1,83	1,86	1,90	1,38	1,60	1,46	1,66	1,54	2,04	2,26	1,70	1,41	1,37
Yb	1,36	1,36	1,38	1,48	1,60	1,51	1,41	1,25	1,39	1,36	1,40	1,37	1,36	1,45	1,32	1,22	1,18
Th	8,70	8,82	9,09	10,18	9,44	9,92	10,15	4,35	6,58	8,70	6,48	6,79	7,54	9,02	7,66	7,70	7,79
$^{87}Sr/^{86}Sr$	0,706870					0,706778	0,706749						0,706566	0,706857			
±	0,000007					0,000008	0,000006						0,000006	0,000007			
$^{143}Nd/^{144}Nd$	0,512304					0,512309	0,512310						0,512346	0,512336			
±	0,000007					0,000004	0,000008						0,000005	0,000005			
$^{206}Pb/^{204}Pb$	18,1880					18,1880	18,1860						18,2438	18,2236			
±	0,0008					0,0005	0,0004						0,0004	0,0003			
$^{207}Pb/^{204}Pb$	15,6130					15,6126	15,6118						15,6139	15,6128			
±	0,0007					0,0005	0,0003						0,0004	0,0003			
$^{208}Pb/^{204}Pb$	38,5640					38,5873	38,5879						38,5477	38,5596			
±	0,0020					0,0012	0,0008						0,0010	0,0008			

1051

1052 **Table 1.** Whole-rock major, trace elements and Sr-Nd-Pb isotopes for the Ubinas.

1053

Table 2. Selected plagioclase analyses for Ubinas samples

Sample	UBI-10-10B	UBI-10-10B	UBI-10-10B	UBI-10-10C	UBI-10-10C	UBI-10-12	UBI-10-12	UBI-10-14	UBI-10-14	UBI-10-14	UBI-10-07	UBI-10-07	UBI-10-07	UBI-10-01	UBI-10-01	UBI-10-01	UBI-10-01	UBI-10-18B	UBI-10-18B	UBI-10-18B	UBI-15-14	UBI-15-14	UBI-15-14	UBI-15-14
Age	>10 ka	>10 ka	>10 ka	>10 ka	>10 ka	2-10 ka	2-10 ka	2-10 ka	2-10 ka	2-10 ka	2-10 ka	2-10 ka	2-10 ka	1-2 ka	1-2 ka	1-2 ka	1-2 ka	2006 CE	2006 CE	2006 CE	2015 CE	2015 CE	2015 CE	2015 CE
Composition	R	R	R	R	R	D	D	D	D	D	D	D	D	A	A	A	A	BA	BA	BA	BA	BA	BA	BA
Analyse	PL3-C	PL3-I	PL3-R	PL1-C	PL1-R	PL5-C	PL6-R	PL5-R	PL3-I	PL5-R	PL5-I	PL3-R	PL3-I	PL9-C	PL9-R	PL9-R	PL9-C	PL1-C	PL1-I	PL1-R	PL3-C	PL3-R	PL3-I	PL5-R
SiO_2 (wt.%)	52,1	55,5	58,6	57,7	57,3	53,8	58,9	58,3	57,3	59,5	56,8	61,1	56,7	52,5	53,8	54,2	53,5	58,3	54,0	52,2	54,0	49,2	56,9	52,5
TiO_2	0,0	0,0	0,0	0,0	0,0	0,1	0,0	0,0	0,0	0,1	0,0	0,0	0,0	0,0	0,0	0,1	0,1	0,0	0,1	0,1	0,1	0,1	0,1	0,1
Al_2O_3	30,7	28,0	26,4	26,5	27,1	29,4	25,3	25,7	26,6	25,4	26,9	25,2	27,4	30,2	29,2	29,2	28,3	25,7	28,1	29,7	28,0	31,3	26,3	29,4
FeO*	0,3	0,3	0,2	0,2	0,2	0,3	0,3	0,3	0,4	0,3	0,3	0,4	0,5	0,5	0,5	0,4	0,3	0,4	0,7	0,7	0,5	0,6	0,6	0,7
MnO	0,0	0,0	0,0	0,0	0,0	0,1	0,0	0,0	0,0	0,0	0,0	0,0	0,0	0,0	0,0	0,0	0,0	0,0	0,0	0,0	0,0	0,0	0,0	0,0
MgO	0,0	0,0	0,0	0,0	0,0	0,0	0,0	0,0	0,0	0,0	0,0	0,0	0,0	0,0	0,0	0,1	0,0	0,0	0,0	0,0	0,1	0,0	0,0	0,0
CaO	13,3	10,3	8,2	8,4	9,0	11,8	7,6	8,0	8,8	7,7	9,7	7,0	9,8	13,2	12,0	11,7	11,3	8,0	11,5	13,3	10,7	15,1	8,5	12,4
Na_2O	3,8	5,3	6,4	6,1	5,8	4,5	6,8	6,3	6,0	6,5	5,8	6,7	5,7	3,9	4,4	4,5	4,9	6,1	4,4	4,0	4,8	2,9	6,1	4,2
K_2O	0,2	0,2	0,4	0,3	0,3	0,3	0,5	0,5	0,5	0,8	0,5	1,0	0,4	0,3	0,3	0,3	0,3	0,6	0,6	0,4	0,5	0,1	0,6	0,3
Total	100,4	99,6	100,3	99,4	99,8	100,1	99,5	99,1	99,6	100,3	100,3	101,5	100,6	100,6	100,4	100,4	98,7	99,4	99,4	100,3	98,7	99,4	99,2	99,7
An (mol%)	65,1	51,3	40,3	42,1	45,1	58,4	36,9	40,3	43,5	37,7	46,7	34,4	47,7	64,1	58,7	57,8	55,0	40,1	56,6	63,7	53,8	73,6	42,0	61,0
Ab	34,0	47,5	57,3	55,5	52,8	40,1	60,2	56,8	53,6	57,9	50,4	59,9	49,8	34,7	39,3	40,4	43,1	55,3	39,7	34,3	43,2	25,5	54,2	37,0
Or	1,0	1,2	2,4	2,3	2,1	1,5	2,9	2,8	2,9	5,6	2,9	5,6	2,5	1,3	1,9	1,8	1,9	4,6	3,7	2,0	3,0	0,9	3,8	1,9

PL: Plagioclase, An: Anorthite, Ab: Albite, Or: Orthoclase, C: Core, I: Interior, R: Rim, a: altered. * all iron as FeO

1054

Table 2. Selected plagioclase analyses for Ubinas samples.

Table 3. Selected amphibole and biotite analyses for Ubinas samples

Sample	UBI-10-10B	UBI-10-10B	UBI-10-10C	UBI-10-10C	UBI-10-12	UBI-10-12	UBI-10-14	UBI-10-14	UBI-10-01	UBI-10-01	UBI-10-01	UBI-10-01	UBI-10-18C	UBI-10-18C	UBI-15-14	UBI-15-14	UBI-10-10B	UBI-10-10B	UBI-10-12	UBI-10-12	UBI-10-07	UBI-10-07
Age	>10 ka	>10 ka	2-10 ka	2-10 ka	2-10 ka	2006 CE	2006 CE	2-10 ka	2-10 ka	1-2 ka	1-2 ka	1-2 ka	2006 CE	2006 CE	2015 CE	2015 CE	>10 ka	>10 ka	2-10 ka	2-10 ka	2-10 ka	2-10 ka
Composition	R	R	R	R	D	D	D	D	A	A	A	A	BA	BA	BA	BA	R	R	D	D	D	D
Analyse	AMPH1-C	AMPH1-R	AMPH2-C	AMPH2-R	AMPH1-C	AMPH1-R	AMPH2-C	AMPH2-R	AMPH1-C	AMPH1-R	AMPH5-C	AMPH5-R	AMPH2-C	AMPH2-R	AMPH4-C	AMPH4-R	BIO5-C	BIO5-R	BIO2-C	BIO2-I	BIO1	BIO
SiO_2 (wt.%)	44,1	45,3	41,4	45,0	40,9	44,4	44,3	44,2	43,6	43,3	41,1	43,8	41,3	41,0	41,9	41,8	37,0434	37,009	36,5126	37,2194	37,3616	36,5603
TiO_2	2,1	1,9	2,9	2,0	3,2	2,3	2,4	2,5	3,0	3,1	3,5	3,0	3,7	3,8	3,6	3,6	4,3865	4,5607	5,203	4,9763	5,6069	5,8029
Al_2O_3	10,3	9,5	12,7	9,2	12,4	9,2	9,7	9,5	10,2	10,4	12,0	10,8	12,7	12,8	12,7	12,3	14,7432	14,4249	13,9496	13,5983	13,8006	13,5493
FeO*	13,1	13,2	12,1	13,0	13,7	13,0	12,8	12,5	12,1	11,7	12,4	12,2	11,6	11,0	10,3		14,4929	14,4106	14,5254	14,8061	13,4399	13,6893
MnO	0,3	0,4	0,2	0,5	0,3	0,5	0,4	0,3	0,3	0,2	0,3	0,1	0,1	0,1	0,1		0,0855	0,217	0,2036	0,2883	0,1416	0,1365
MgO	13,5	13,8	13,4	13,8	12,7	13,6	13,9	13,7	14,4	14,2	13,5	14,2	14,6	14,2	14,2	14,6	14,9329	14,7419	14,3808	14,9171	15,3057	15,0024
CaO	11,3	11,4	11,4	11,2	11,3	11,1	11,2	11,1	10,9	11,3	11,5	11,6	11,6	11,4	11,3		0,0063	0,6238	0,078	0,0534	0,0425	0,0614
Na_2O	2,0	1,8	2,3	1,9	2,3	2,0	2,0	2,0	2,1	2,2	2,2	2,1	2,6	2,5	2,4		0,6892	0,6238	0,6307	0,5559	0,6143	0,624
K_2O	0,8	0,8	0,7	0,7	0,7	0,7	0,7	0,8	0,8	0,8	0,7	0,9	0,8	0,8	0,8		8,5793	8,5517	8,857	8,949	8,9515	9,0165
Total	97,4	98,0	97,0	97,3	97,5	97,0	97,5	97,0	97,5	97,0	97,1	98,9	97,3	97,5	98,1	97,2	95,3159	94,59	94,3694	95,3569	95,2645	94,4738
Mg#	64,7	65,0	66,4	65,4	62,3	65,0	65,9	66,1	68,1	68,5	65,9	67,5	72,7	70,4	69,7	71,5	-	-	-	-	-	-

AMPH: Amphibole, BIO: Biotite, C: Core, I: Interior, R: Rim. * all iron as FeO

1056

Table 3. Selected amphibole and biotite analyses for Ubinas samples.

Table 4. Selected clinopyroxene and orthopyroxene analyses for Ubinas samples

Sample	UBI-10-07	UBI-10-07	UBI-10-19A	UBI-10-19A	UBI-10-19A	UBI-10-18B	UBI-10-18B	UBI-10-18B	UBI-15-14	UBI-15-14	UBI-15-14	UBI-15-14	UBI-15-14	UBI-10-07	UBI-10-07	UBI-10-01	UBI-10-01	UBI-10-01	UBI-10-01	UBI-10-18B	UBI-10-18B
Age	2-10 ka	2-10 ka	1667 CE	1667 CE	1667 CE	2006 CE	2006 CE	2006 CE	2015 CE	2015 CE	2015 CE	2015 CE	2015 CE	2-10 ka	2-10 ka	1-2 ka	1-2 ka	1-2 ka	1-2 ka	2006 CE	2006 CE
Composition	D	D	BA	BA	BA	BA	BA	BA	BA	BA	BA	BA	BA	D	D	A	A	A	A	BA	BA
Analyse	CPX2-C	CPX2-R	CPX3-C	CPX3-R	CPX2-R	CPX1-C	CPX1-R	CPX1-I	CPX1-C	CPX1-R	CPX1-C	CPX1-R	CPX6-R	OPX2-C	OPX2-R	OPX1-C	OPX1-I	OPX1-R	OPX1-R	OPX2-C	OPX2-R
SiO_2 (wt.%)	53,3	53,2	51,2	51,5	50,3	51,8	52,4	51,9	51,4	49,6	50,3	51,2	52,7	54,1	53,5	54,5	54,2	54,1	54,5	54,8	52,8
TiO_2	0,2	0,5	0,6	0,9	1,2	0,7	0,7	0,7	0,5	1,0	1,1	0,9	0,6	0,1	0,1	0,2	0,2	0,2	0,2	0,3	0,5
Al_2O_3	1,1	2,2	1,9	3,5	3,2	2,0	1,9	2,4	2,0	4,8	3,8	2,7	1,6	0,6	0,6	0,9	0,9	0,9	0,9	0,8	1,2
FeO*	7,9	8,6	14,1	6,7	8,8	9,6	9,3	9,1	12,0	9,0	8,8	8,2	8,4	19,7	19,9	17,5	17,6	17,8	16,9	15,3	16,9
MnO	0,5	0,5	0,4	0,1	0,2	0,3	0,3	0,4	0,3	0,1	0,2	0,2	0,3	1,3	1,2	0,7	0,8	0,9	0,7	0,4	0,5
MgO	14,9	15,4	14,1	16,0	15,2	15,3	16,1	15,3	16,1	13,5	13,7	14,5	15,9	23,7	23,6	25,6	25,7	25,4	25,6	26,9	24,2
CaO	21,9	21,3	19,2	20,9	19,7	19,8	20,0	19,0	19,6	21,2	21,0	20,8	19,8	0,9	1,0	1,1	1,1	1,1	1,1	1,6	2,2
Na_2O	0,4	0,3	0,5	0,5	0,4	0,4	0,4	0,3	0,6	0,4	0,4	0,3	0,3	0,0	0,0	0,0	0,0	0,0	0,1	0,1	0,1
K_2O	0,0	0,0	0,0	0,0	0,0	0,0	0,0	0,0	0,0	0,0	0,0	0,0	0,0	0,0	0,0	0,0	0,0	0,0	0,0	0,0	0,0
Total	100,2	102,2	99,9	100,7	99,6	99,9	100,3	99,8	100,2	99,9	99,7			100,4	99,8	100,5	100,5	99,9	99,9	100,0	98,5
En (mol%)	42,0	43,0	40,5	46,0	44,9	43,5	43,6	46,0	39,1	40,3	41,8	43,9	45,4	65,5	65,3	69,9	69,8	69,2	70,7	73,0	68,0
Fs	13,3	14,2	19,9	10,9	14,5	15,8	15,4	15,1	20,1	15,0	14,6	13,5	14,0	32,7	32,7	27,9	28,0	28,5	27,2	23,8	27,5
Wo	44,7	42,8	39,6	43,1	40,6	40,7	41,0	38,9	40,8	44,8	43,6	42,6	40,6	1,8	2,0	2,2	2,2	2,3	2,1	3,2	4,5
Mg#	77,1	76,2	67,8	81,1	76,1	73,9	74,6	75,9	66,6	73,2	74,6	76,9	77,1	68,1	67,9	72,3	72,3	71,8	73,0	75,9	71,9

CPX: Clinopyroxene, OPX: Orthopyroxene, EN: Enstatite, Fe: Ferrosilite, Wo: Wollastonite, C: Core, I: Interior, R: Rim. * all iron as FeO

1058

Table 4. Selected clinopyroxene and orthopyroxene analyses for Ubinas samples.

Table 5. Selected olivine and Fe-Ti oxides analyses for Ubinas samples

Sample	UBI-10-18C	UBI-10-18C	UBI-10-18C	UBI-15-14	UBI-15-14	UBI-10-10B	UBI-10-10B	UBI-10-07	UBI-10-07	UBI-10-07	UBI-10-07	UBI-10-01	UBI-10-18C
Age	2006 CE	2006 CE	2006 CE	2015 CE	2015 CE	14 ka	14 ka	1-7 ka	1-7 ka	1-7 ka	1-7 ka	1 ka	2006-2009
Composition	BA	BA	BA	BA	BA	R	R	D	D	D	D	A	BA
Analyse	OL1-C	OL1-I	OL1-R	OL1-C	OL1-R	MAG1-C	MAG2-C	ILM2	MAG3	ILM3	MAG4	MAG1-C	MAG3
SiO_2 (wt.%)	38,9	38,9	38,0	37,8	37,1	0,1	0,1	0,0	0,1	0,0	0,0	0,0	0,1
TiO_2	0,0	0,0	0,0	0,0	0,0	5,8	6,0	37,5	7,1	38,2	7,3	8,9	15,7
Al_2O_3	0,0	0,0	0,0	0,0	0,0	1,8	1,7	0,3	1,8	0,3	1,8	2,7	2,7
FeO*	20,6	20,9	24,6	28,7	30,0	84,0	84,3	54,8	82,2	54,9	82,7	79,8	73,7
MnO	0,3	0,2	0,5	0,5	0,7	0,7	0,8	0,6	0,5	0,5	0,5	0,5	0,5
MgO	40,2	39,8	36,5	34,4	32,1	1,1	1,1	2,4	1,8	2,5	1,6	2,6	3,3
CaO	0,1	0,1	0,2	0,1	0,2	0,1	0,0	0,0	0,0	0,0	0,1	0,0	0,0
Na_2O	0,0	0,0	0,0	0,0	0,0	0,0	0,0	0,0	0,0	0,0	0,0	0,0	0,0
K_2O	0,0	0,0	0,0	0,0	0,0	0,0	0,0	0,1	0,0	0,0	0,0	0,0	0,0
Total	100,3	99,9	99,8	101,6	100,2	93,6	94,0	95,7	93,6	96,5	94,2	94,6	96,2
Fo (mol%)	77,7	77,2	72,5	68,1	65,6	-	-	-	-	-	-	-	-

OL: Olivine, MAG: Magnetite; IL: Ilmenite, Fo: Forsterite, C: Core, I: Interior, R: Rim. * all iron as FeO

1060

Table 5. Selected olivine and Fe-Ti oxides analyses for Ubinas samples.

Table 6. Matrix glass composition (average ± standard deviation) for Ubinas samples

Sample	UBI-10-10B	UBI-10-10C	UBI-10-12	UBI-10-14	UBI-10-07	UBI-10-01	UBI-10-19A	UBI-10-18C	UBI-10-18B
Age	>10 ka	>10 ka	2-10 ka	2-10 ka	2-10 ka	1-2 ka	1667 CE	2006 CE	2006 CE
No. Analyses	6	8	6	6	12	13	5	11	3
SiO_2 (wt.%)	71.6 ±0.4	71.4 ±0.6	73.0 ±0.7	70.8 ±0.3	71.9 ±0.6	66.9 ±1.4	62.4 ±0.8	65.7 ±1.2	69.1 ±1.4
TiO_2	0.2 ±0.1	0.2 ±0.1	0.2 ±0.1	0.2 ±0.1	0.3 ±0.1	0.5 ±0.1	1.8 ±0.2	1.6 ±0.2	0.7 ±0.3
Al_2O_3	13.8 ±0.2	13.4 ±0.3	13.0 ±0.2	13.7 ±0.2	13.1 ±0.3	15.0 ±0.4	14.6 ±0.3	14.5 ±0.5	14.7 ±0.3
FeO*	1.1 ±0.1	1.1 ±0.1	1.0 ±0.2	1.2 ±0.1	1.2 ±0.1	2.4 ±0.3	5.5 ±0.4	4.4 ±0.3	2.4 ±0.3
MnO	0.1 ±0.1	0.1 ±0.1	0.1 ±0.05	0.05 ±0.05	0.1 ±0.05	0.1 ±0.1	0.2 ±0.1	0.1 ±0.1	0.05 ±0.05
MgO	0.2 ±0.05	0.2 ±0.05	0.2 ±0.1	0.2 ±0.1	0.2 ±0.05	0.7 ±0.1	1.9 ±0.1	0.9 ±0.05	0.3 ±0.2
CaO	1.3 ±0.1	1.2 ±0.1	0.9 ±0.2	1.1 ±0.1	1.0 ±0.1	2.9 ±0.8	3.6 ±0.3	2.0 ±0.3	5.4 ±1.5
Na_2O	3.4 ±0.6	4.1 ±0.1	3.3 ±0.3	3.7 ±0.2	3.1 ±0.5	3.7 ±0.9	4.8 ±0.2	4.4 ±0.3	1.1 ±0.8
K_2O	4.1 ±0.3	3.8 ±0.1	4.6 ±0.3	4.7 ±0.2	5.1 ±0.3	4.0 ±0.4	4.0 ±0.4	5.2 ±0.3	3.6 ±0.7
Total	95,8	95,4	96,2	95,8	96,0	96,3	98,7	98,9	97,2

* all iron as FeO

1062

1063   **Table 6.** Matrix glass composition (average ± standard deviation) for Ubinas samples.

	BA	A	D	R	Method
T [ºC]	884 ± 23 (13)	881 ± 5 (6)	787 ± 11 (5)	813 ± 5 (8)	Pl-melt, Putirka (2008)
	-	-	879 ± 4 (9)	849 ± 3 (2)	Mag-Ilm, Lindsley and Spencer (1982)
	-	913 ± 13 (15)	881 ± 36 (21)	846 ± 30 (12)	Hb-Pl, Holland and Blundy (1994)
	994 ± 9 (23)	933 ± 16 (26)	880 ± 35 (29)	894 ± 37 (16)	Al^T in amph, Ridolfi et al. (2010)
	993 ± 24 (8)	-	-	-	Two-pyroxenes, Putirka (2008)
P [MPa]	583 ± 17 (23)	426 ± 40 (26)	318 ± 109 (29)	385 ± 95 (16)	Al-in-hb, Johnson and Rutherford (1989)
	453 ± 26 (23)	267 ± 42 (26)	197 ± 81 (29)	242 ± 84 (16)	Al^T in amph, Ridolfi et al. (2010)
	357 ± 138 (23)	218 ± 26 (26)	145 ± 63 (29)	161 ± 51 (16)	Al^T in amph, Ridolfi and Renzulli (2012)
	341 ± 35 (23)	246 ± 28 (26)	241 ± 31 (29)	316 ± 51 (16)	^{VI}Al in amph, Medard and Le Pennec (2019)
H_2O [wt.%]	5.0 ± 0.3 (23)	4.3 ± 0.3 (26)	4.6 ± 0.3 (29)	5.3 ± 0.4 (16)	Al^T in amph, Ridolfi and Renzulli (2012)

1064

1065   **Table 7.** T-P-H_2O conditions for Ubinas magmas.

Supplementary material 1. Samples location for Ubinas volcano

| Sample No.	Estimated Age	Stratigraphic position	UTM North[*]	UTM East[*]	Altitude[**]	Locality	Observations
UBI-10-10A	< 10 ka	1	8184760	300284	3646	Sacuhaya	Pumice on tephra fallout deposit
UBI-10-10B	< 10 ka	1	8184760	300284	3646	Sacuhaya	Pumice on tephra fallout deposit
UBI-10-10C	< 10 ka	1	8184760	300284	3646	Sacuhaya	Pumice on tephra fallout deposit
UBI-10-11	2-10 ka	2	8184760	300284	3646	Sacuhaya	Pumice on tephra fallout deposit
UBI-10-07	2-10 ka	3	8187865	302316	3552	Qda. Infiernillos	Pumice on tephra fallout deposit
UBI-10-12	2-10 ka	4	8184760	300284	3646	Sacuhaya	Pumice on tephra fallout deposit
UBI-10-13	2-10 ka	5	8184760	300284	3646	Sacuhaya	Pumice on tephra fallout deposit
UBI-10-14	2-10 ka	6	8184760	300284	3646	Sacuhaya	Pumice on tephra fallout deposit
UBI-10-15	2-10 ka	7	8184760	300284	3646	Sacuhaya	Pumice on tephra fallout deposit
UBI-10-08	2-10 ka	7	8187865	302316	3552	Qda. Infiernillos	Pumice on tephra fallout deposit
UBI-10-16	2-10 ka	8	8184760	300284	3646	Sacuhaya	Pumice on tephra fallout deposit
UBI-10-09	2-10 ka	9	8187865	302316	3552	Corohuayo	Pumice on tephra fallout deposit
UBI-13-05	2-10 ka	10				Qda. Infiernillos	Pumice on tephra fallout deposit
UBI-10-01A	1-2 ka	11	8188321	301606	3498	Qda. Infiernillos	Pumice on tephra fallout deposit
UBI-10-01B	1-2 ka	11	8188321	301606	3498	Qda. Infiernillos	Pumice on tephra fallout deposit
UBI-10-02	1-2 ka	11	8188321	301606	3498	Qda. Infiernillos	Pumice on tephra fallout deposit
UBI-10-03	1-2 ka	11	8188321	301606	3498	Qda. Infiernillos	Pumice on tephra fallout deposit
UBI-10-04	1-2 ka	11	8188321	301606	3498	Qda. Infiernillos	Pumice on tephra fallout deposit
UBI-10-05	1-2 ka	11	8188321	301606	3498	Qda. Infiernillos	Pumice on tephra fallout deposit
UBI-14-01A	1-2 ka	11	8191605	301958	4065	Ubinas-Para road	Pumice on tephra fallout deposit
UBI-10-06	1-2 ka	12	8188321	301606	3498	Qda. Infiernillos	Pumice on tephra fallout deposit
UBI-14-01C	1-2 ka	12	8191605	301958	4065	Ubinas-Para road	Pumice on tephra fallout deposit
UBI-14-01B	1-2 ka	12	8191605	301958	4065	Ubinas-Para road	Pumice on tephra fallout deposit
UBI-10-19	1667 CE	13	8192554	296907	5432	Upper flank	lava block on PDC
UBI-10-20	2006-2009 CE	14				Upper flank	Ballistic block
UBI-10-18A	2006-2009 CE	14	8192025	296976	5407	Caldera inside	Ballistic block
UBI-10-18B	2006-2009 CE	14	8192025	296976	5407	Caldera inside	Ballistic block
UBI-10-18C	2006-2009 CE	14	8192025	296976	5407	Caldera inside	Ballistic block
UBI-14-12	2014-2015 CE	15				Upper flank	Ballistic block
UBI-14-04	2014-2015 CE	15				Upper flank	Ballistic block
UBI-14-03	2014-2015 CE	15				Upper flank	Ballistic block
UBI-15-14	2014-2015 CE	15				Upper flank	Ballistic block
UBI-15-02	2014-2015 CE	15				Upper flank	Ballistic block

[*] WGS84
[**] meters above sea level

1066

1067 **Supplementary material 1.** Samples location for Ubinas volcano.

1068

1069 **Supplementary material 2.** Mineral composition for Ubinas samples.
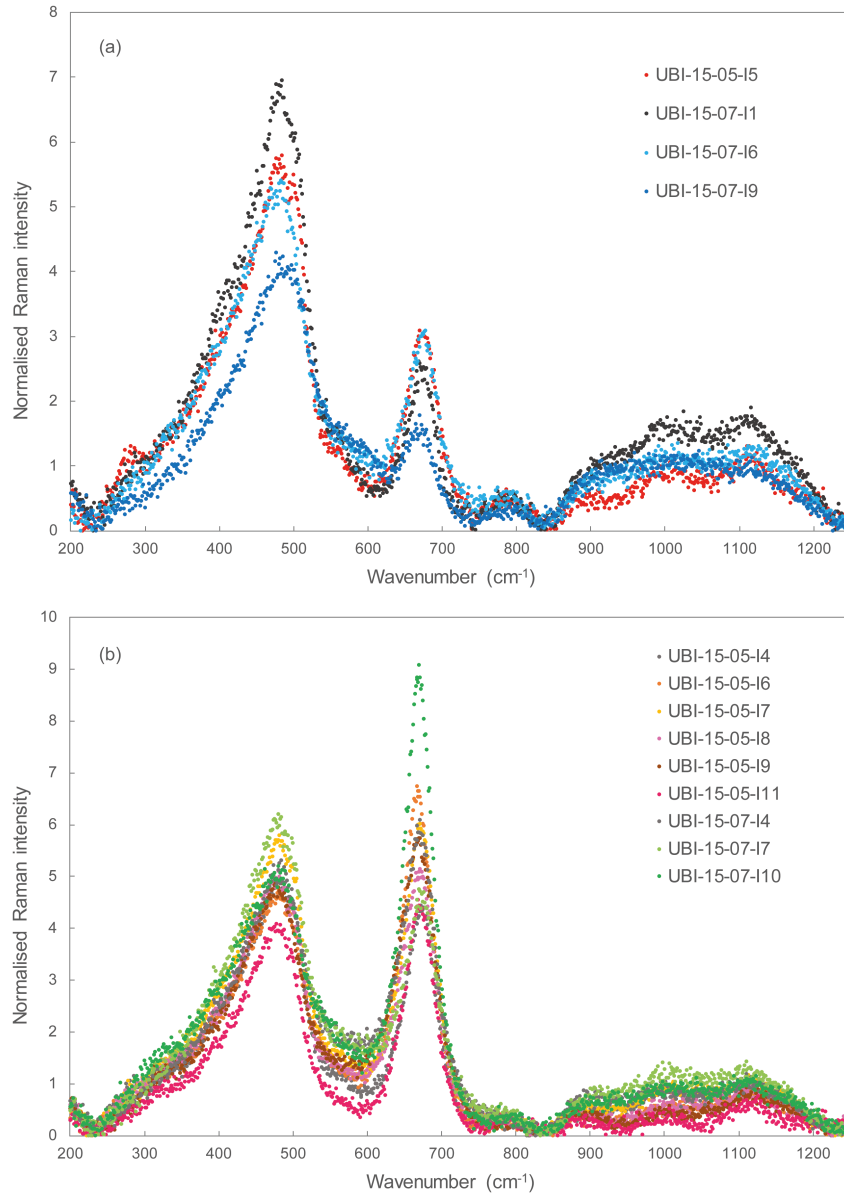
1070

1071 **Supplementary material 3.** Raman spectra showing the glass bands in the alumino-silicate network domain. The

1072 intense peak at ~ 670 cm^{-1} indicates the presence of magnetite nanolites dispersed in the glass. **(a)** Spectra of

1073 selected inclusions only slightly affected by the presence of magnetite (intensity ratios of magnetite peak to glass

1074 band ranging from 0.4 to 0.6). **(b)** Spectra of glass inclusions strongly affected by the presence of magnetite

1075 (intensity ratios from 0.6 to 1.8). Signal intensity is normalized to acquisition time and laser power.

1076

1077
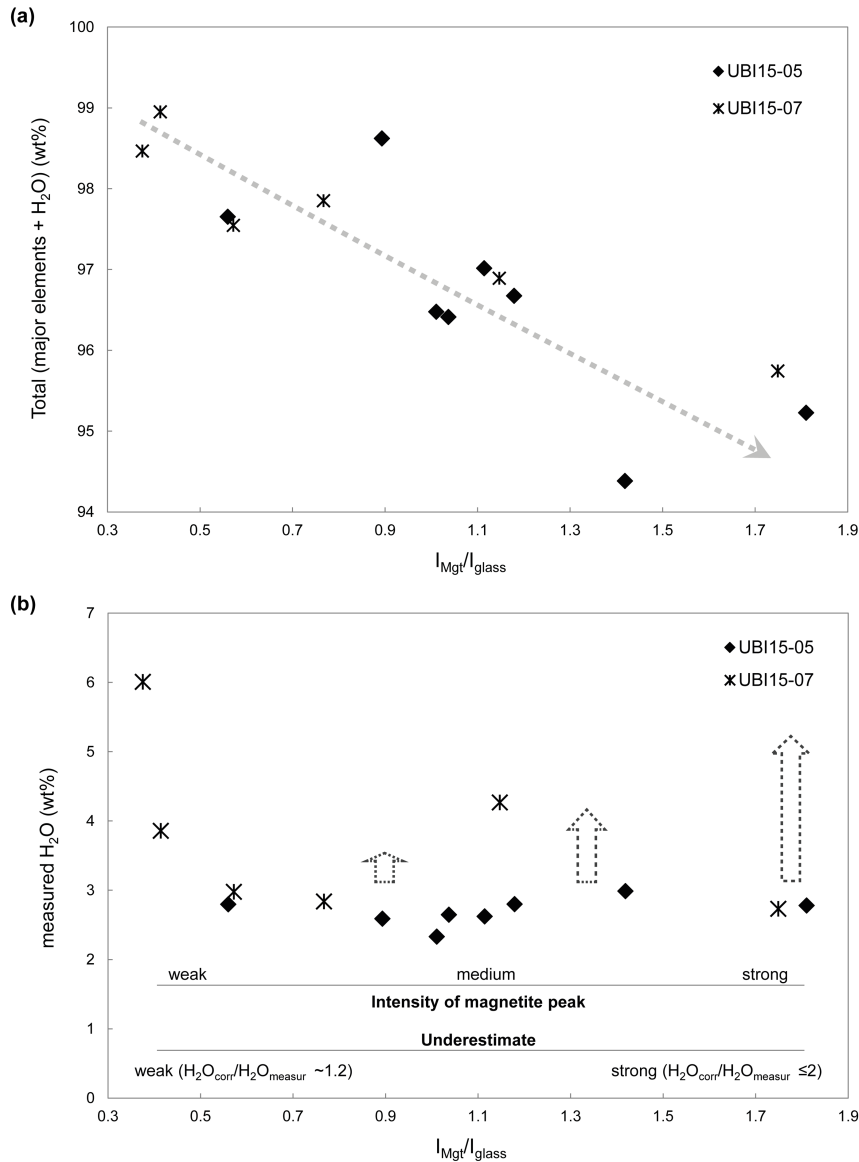
1078

Supplementary material 4. Effect of the presence of magnetite nanolites on the quantification of water in glass

inclusions by Raman spectroscopy. I_{Mgt}/I_{glass} is the ratio of the intensity of the main Raman peak of magnetite to

the intensity of the principal Raman band of the glass. **(a)** Plot of I_{Mgt}/I_{glass} versus the totals calculated as the sum

of all major elements measured by electron microprobe and H_2O values measured by Raman spectroscopy. A

negative correlation is observed, indicating that the measured water content is more accurate for inclusions weakly

affected by the presence of magnetite (low I_{Mgt}/I_{glass}) and that low totals are due to underestimate of the water

contents for high I_{Mgt}/I_{glass}. **(b)** Plot of I_{Mgt}/I_{glass} versus the measured water contents. For low I_{Mgt}/I_{glass}, the measured

water contents are not or weakly underestimated, whereas they deviate progressively from the correct contents as

the I_{Mgt}/I_{glass} ratio increases. The three dashed arrows indicate the approximate extent of the correction needed to

obtain the true water contents.
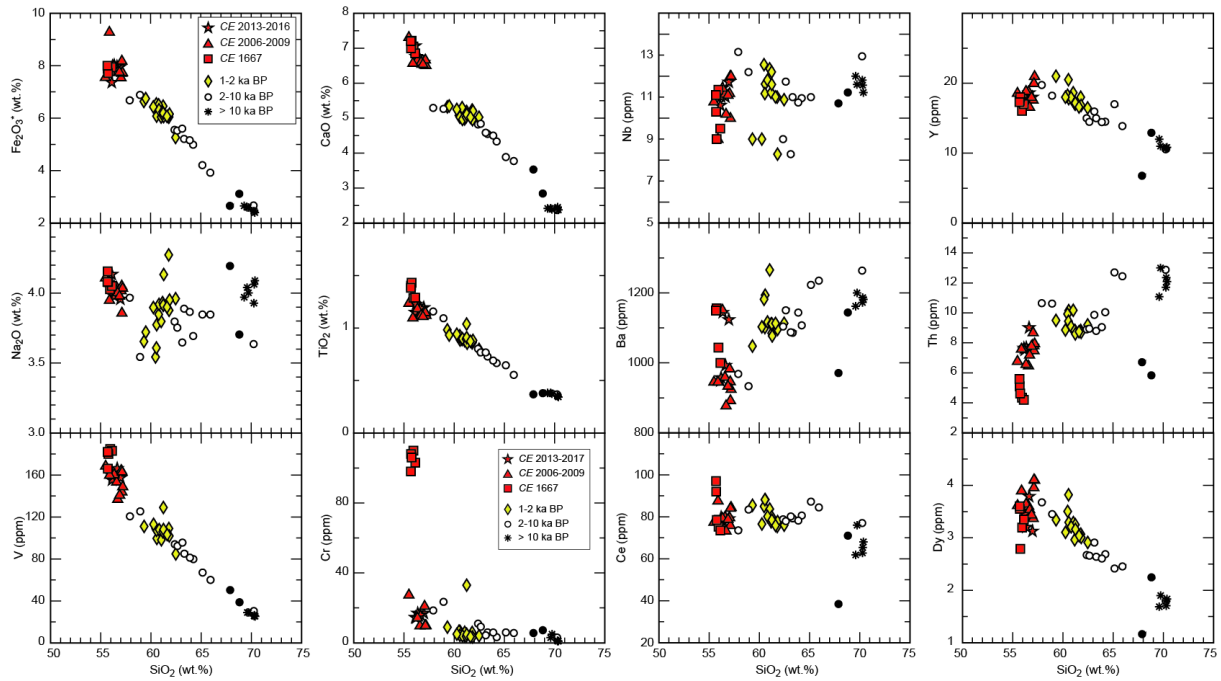
1089

Supplementary material 5. Binary diagrams of the Ubinas magmatic series, showing major (Fe$_2$O$_3$*, CaO, Na$_2$O,

1091 TiO$_2$) and trace elements (V, Cr, Nb, Y, Ba, Th, Ce, Dy) plotted against silica as a differentiation index.
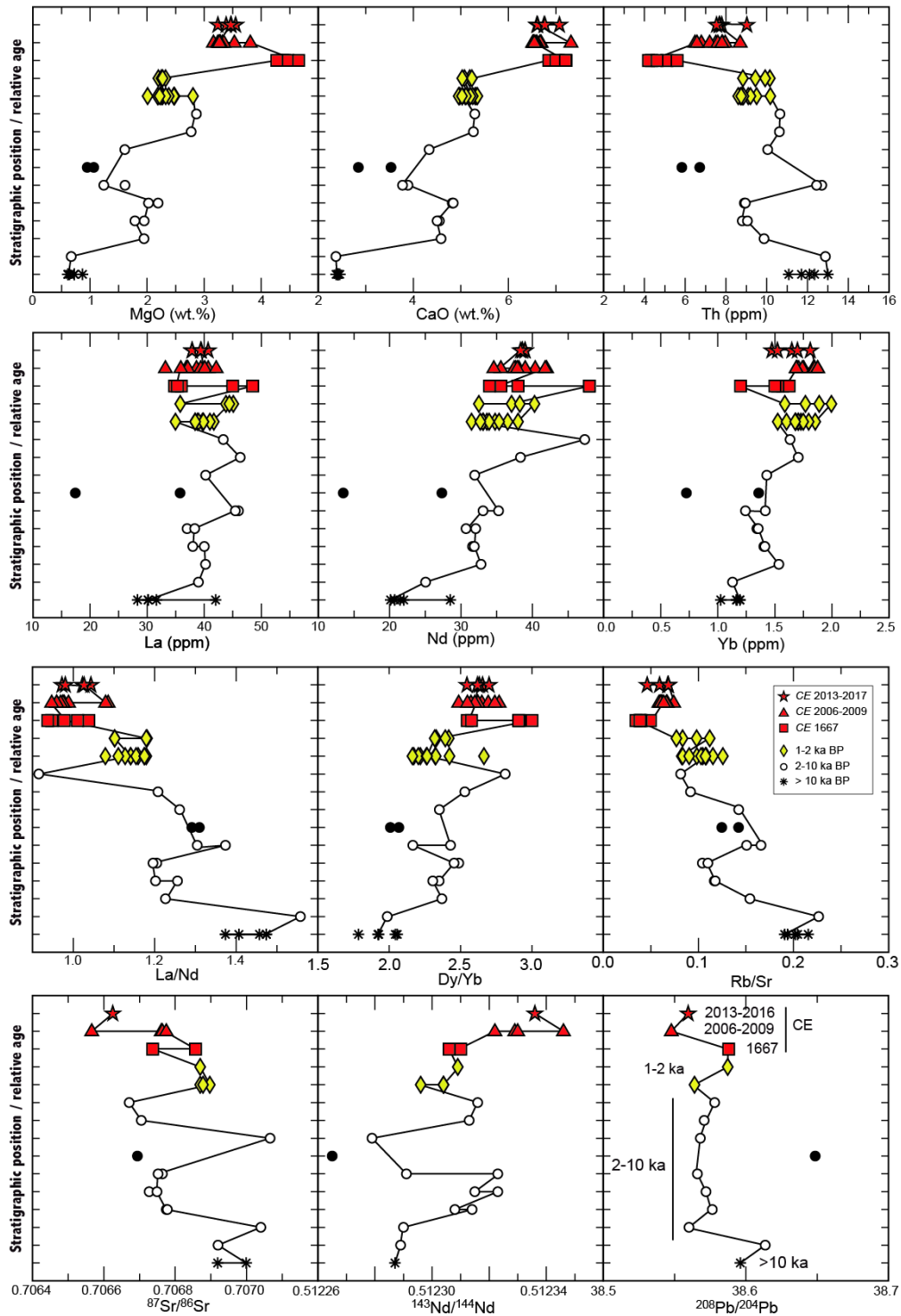
1092

Supplementary material 6. Temporal variation of the Ubinas magmatic series, showing some key major (MgO
and CaO), trace elements concentrations (Th, La, Nd, Yb) and ratios (La/Nd, Dy/Yb, Rb/Sr), as well as some
isotopic ratios (^{87}Sr/^{86}Sr, ^{143}Nd/^{144}Nd, ^{208}Pb/^{204}Pb).

1093

1094

1095

1096